scientific reports

OPEN

Assessment of lithium potential for future exploration in the Ghahavand Plain of Western Iran

Narges Daneshvar[1,2], Hossein Azizi[1✉], Masayo Minami[2], Yoshihiro Asahara[3] & Motohiro Tsuboi[4]

In recent years, numerous countries worldwide have initiated lithium (Li) exploration as a key strategy. In Iran, the Ghahavand Plain, situated in the center of the Hamadan region, has been identified as a prominent site for lithium exploration. A key feature of the Ghahavand Plain sediments is that they contain lithium-bearing minerals, zabuyelite (lithium carbonate) and psedoeucrptite which are rare Lithium aluminum silicate mineral typically associated with Lithium-rich pegmatites. The Li concentration in this area varies from 30 to 102 ppm, with an average of 55.1 ppm. The $^{87}Sr/^{86}Sr$ ratios, ranging from 0.7078 to 0.7103, align with those found in the Alvand granites and the Eocene-Oligocene volcanic rocks, and Oligo-Miocene limestone in the surrounding area. In addition, the chemical index of alteration (CIA), averaging 59.7, indicates an intermediate to felsic rock source for the sediments. The low Ga/Rb ratio (0.18 to 0.27) and high Sr/Cu ratio (8.9 to 710) confirms a cool-arid climate with low temperatures and minimal precipitation conditions during the sedimentation. Furthermore, the lower V/(V + Ni) ratio, ranging from 0.53 to 0.76, suggests a weakly oxidizing environment. Several samples from the northern region of the Ghahavand Plain have elevated Lithium concentrations, in the range of 71 to 102 ppm which is close to the lower limit of lithium-bearing deposits worldwide. Therefore, this area could be considered a potentially promising site for future lithium exploration in Iran. in addition, this study highlights the distribution of lithium within the clay plain in western Iran, and the interest in evaluating resource and tracing weathering.

Keywords Lithium, Clay flat, Paleoenvironment, Hamedan, Iran

Lithium is the lightest alkaline element and is used in various applications, including batteries, pharmaceuticals, ceramics, glass, optics, and more[1,2]. The increasing demand for electric and hybrid vehicles has led to a significant increase in the consumption of lithium minerals, prompting many countries to classify lithium as a critical element[3]. Present global potentials of Lithium include continental brines and associated evaporites, which together account for 58% of the world's lithium reserves[4] and hard-rock pegmatite (lithium-enriched granite), which accounts for 26%, making it the second economically significant lithium resource[5]. Lithium clay (hectorite) accounts for 7%, followed by oilfield brine, geothermal brine, and lithium-zeolite (jadarite) at 3% [6]. A novel type of Li-rich claystone deposit has been identified, exhibiting a relationship to the carbonate weathering process[6]. Other lithium minerals include spodumene ($LiAl(SiO_3)_2$), petalite ($LiAlSi_4O_{10}$), lepidolite ($KLiAl_2Si_3O_{10}(OH, F)$), amblygonite (($LiAlPO_4(F, OH)$)), zinnwaldite ($K(Li, Al, Fe)_3(Al, Si)_4O_{10}(F, OH)_2$), and eucryptite ($LiAlSiO_4$). Lithium compounds like carbonate, chlorite, and hydroxide are commonly associated with evaporite deposits or salt lakes[5].

In recent years, lithium clay-type products have been meticulously designed for specific applications[7]. Lithium clay, particularly hectorite clay, has been identified as a potential future resource[8]. Hectorite, a clay mineral named after its discovery in Hector, California, contains approximately 0.5% lithium[9]. It is a lithium magnesium smectite clay mineral, which is composed of $Na_{0.3}(Mg, Li)_3Si_4O_{10}(OH)_2$[10] and is formed by the alteration of volcanic ash, pumice, and ignimbrites by hydrothermal fluids; this rock formation is known as hydrothermal breccia[11].

[1]Department of Mining Engineering, Faculty of Engineering, University of Kurdistan, Sanandaj 66177-15175, Iran. [2]Division for Chronological Research, Institute for Space–Earth Environmental Research, Nagoya University, Nagoya 464-8601, Japan. [3]Department of Earth and Environmental Science, Graduate School of Environmental Studies, Nagoya University, Nagoya 464-8601, Japan. [4]Department of Applied Chemistry for Environment, School of Biological and Environmental Sciences, Kwansei Gakuin University, Sanda 669-1330, Japan. ✉email: azizi1345@gmail.com; h.azizi@uok.ac.ir

Previously, the proportion of clay-type lithium was relatively low, and extracting lithium from these resources was seen as uneconomical because of technological hurdles and high costs[12]. Although the extraction of lithium from clay-type resources involves a difficult process. The recent discovery of several great clay-lithium deposits in Yunnan, China, has refocused attention on these resources as a viable alternative to conventional lithium sources, such as brine and hard rock deposits[12]. Iran, with its semi-arid climate, has a promising opportunity for the formation of evaporative deposits.

The clay flat in the Ghahavand area (this study), located in the eastern part of Hamedan, Iran, presents a unique geomorphological landscape (Figs. 1 and 2). This region, defined by its vast plains and playas, has been molded by diverse geological and climatic influences[13]. The area is primarily composed of young Quaternary alluvial fans and floodplains, which have been influenced by hydro-geomorphological and morphodynamical processes[13]. The clay expanses, coupled with features like salt flats and pediment cones, highlight the desert nature of the region. These geomorphological markers differentiate desert landscapes from non-desert ones, positioning Ghahavand as a crucial area for exploring desertification and sustainable development.

Key concepts from geological models for lithium-bearing clay deposits used in exploration include the identification of young sedimentary basins with the potential to contain clays derived from felsic volcanic rocks[14]. In this research, we focus on the Ghahavand clay flat as a potential of Li in western Iran. This research investigates the elemental distribution and the controlling factors of Li with a focus on sediment provenance, weathering conditions, and depositional environment. Thirty samples were selected from different areas of this plain to analyze the mineralogical, chemical, and Sr isotopic compositions, the results of which are discussed in this work. Furthermore, based on the whole-rock chemistry and Sr isotopic compositions, the environment and genesis of these deposits are also discussed.
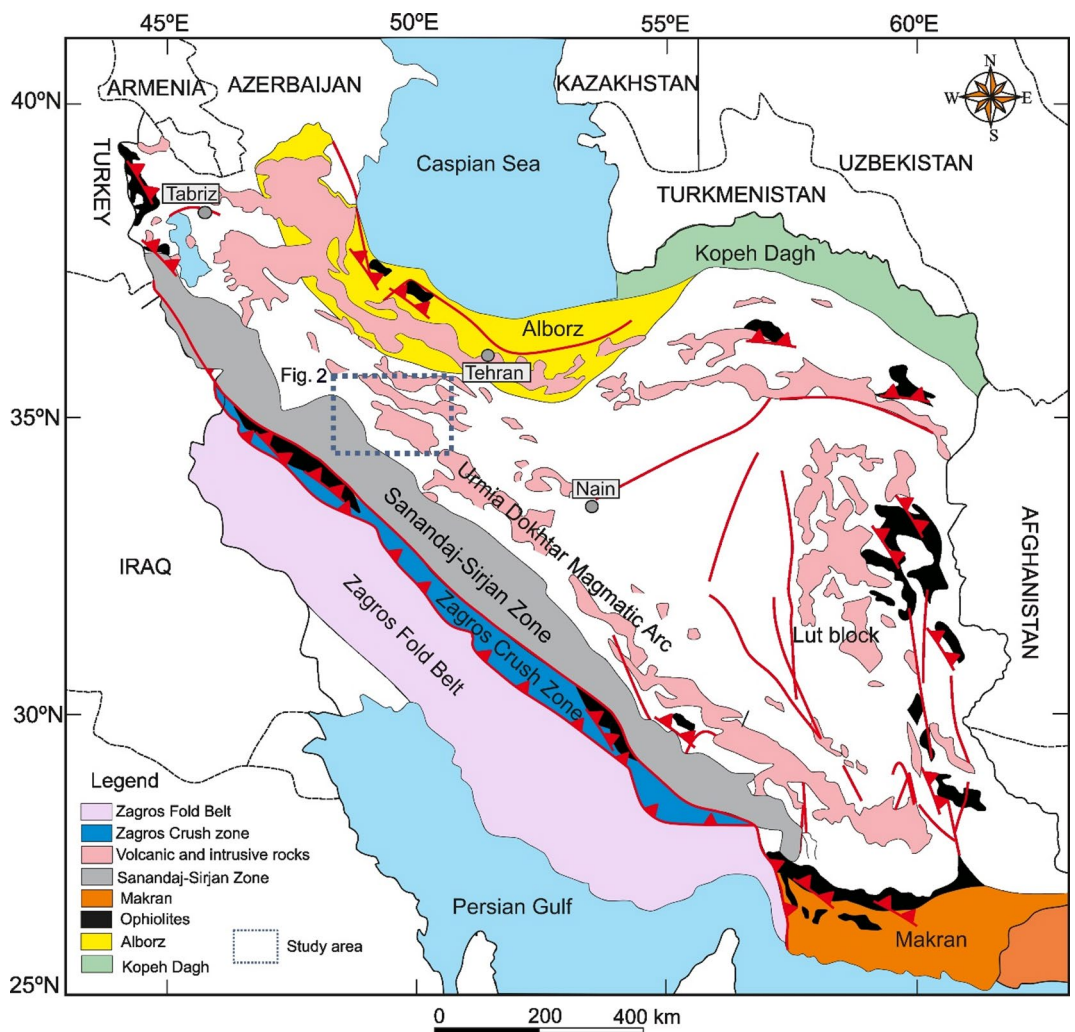

Fig. 1. Simplified geological units of Iran [14] with the location of the study area. The Map was created using ArcGIS Pro online for windows version 3.5.2 (https://www.arcgis.com).
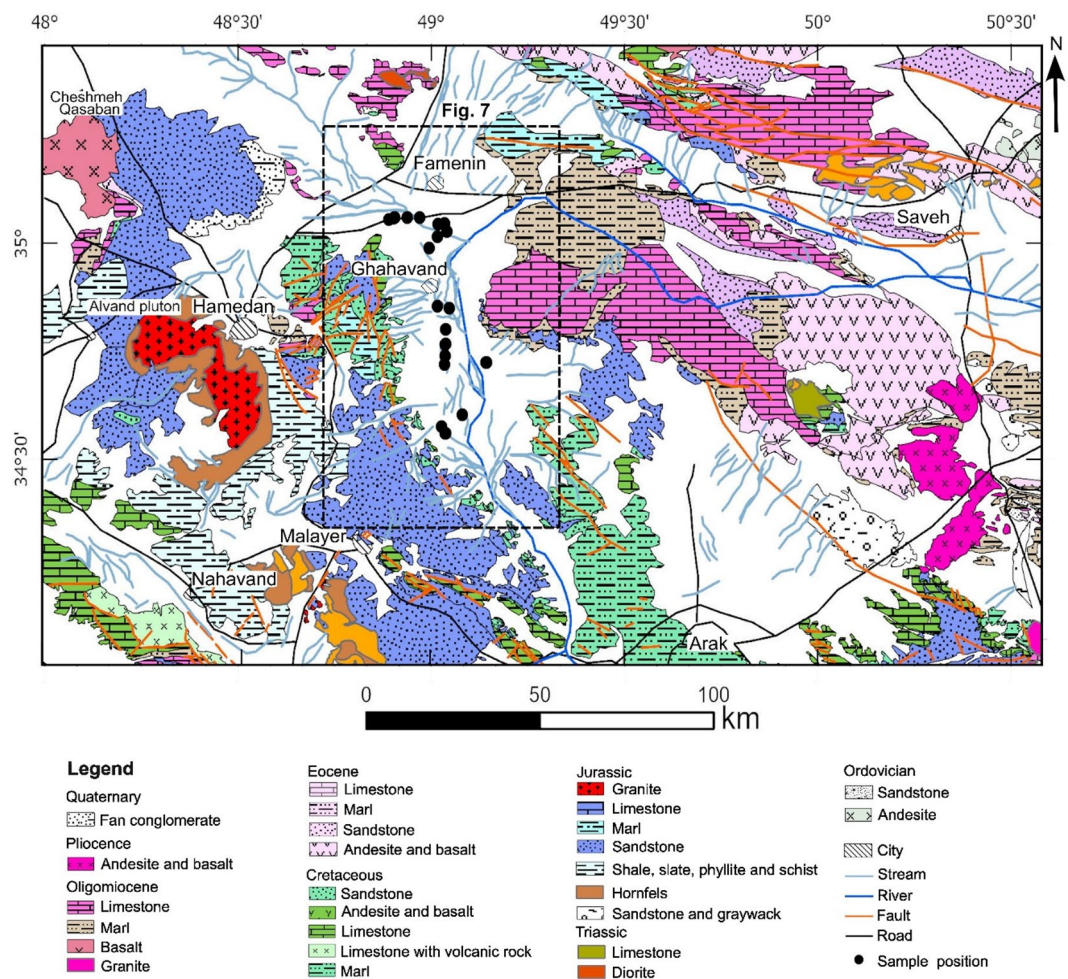
Fig. 2. Simplified geological map of the study area, modified from four 1:250000 geological maps: Qom[17], Kabudar Ahang [18], Saveh [19], and Hamedan [20] . The map was created using ArcGIS Pro online for windows version 3.5.2 (https://www.arcgis.com) and Inkscape for Mac version 1.3.2 (http://Inkscape.en.softonic.com). The modifications include unifying identical layers with the same symbols in the legend, as the map was compiled by merging four 1:25,000 geological maps (Qom, Kabudar Ahang, Saveh, and Hamedan).

Geological setting

The Ghahavand desert spans roughly 3,172 km^2 in Hamedan Province, nestled between the Sanandaj-Sirjan Zone (SaSZ) and the Urmia-Dokhtar magmatic arc in western Iran (Fig. 1)[15]. The Ghahavand Plain boasts a diverse geomorphology, showcasing elements such as alluvial fans, pediment cones, and expansive playas[13]. These formations reveal the hydro-geomorphological and morphodynamic processes that have shaped the region[13].

The peak reaches an impressive height of about 1,704 m, while the base sits at around 1,607 m, giving us a striking height difference of 97 m. The general slope direction is from north to south[13]. In the northern and eastern part of the Ghahavand Plain, there are sequences of Oligocene limestone, Qom Formation, and Miocene Marl, interspersed with halite and gypsum overlanded by low-level piedmont fan and valley terrace deposits, which have a thickness of 70 to 120 m[15]. The soil salinity in the Ghahavand region was assessed using the Normalized Differential Salinity Index (NDSI) based on Landsat 8 OLI data. The results showed that approximately 18% of the area was affected by salinity before 2013, while this percentage increased to 65% in 2019 [16].

The Alvand pluton, along with its surrounding metamorphic complex, is situated on the western side of the Ghahavand Plain. It is one of the largest formations in the central SaSZ, showcasing a diverse array of rock types. Of particular interest is the presence of two-mica, garnet-bearing granite with an S-type signature. Zircon U–Pb dating indicates that the S-type granite crystallized between 170 and 163 million years ago[16]. Pegmatite veins were identified that contain large crystals of spodumene, tourmaline, and apatite, along with quartz, beryl, tourmaline, and apatite[17]. The δ^{6}Li values of spodumene, ranging from + 5.6 to +6.6‰, are indicative of the incorporation of a continental crustal component in their genesis[17]. Aplitic and pegmatitic dykes and bodies have been observed to truncate both the plutonic rocks of the Alvand pluton and its metamorphic aureole. Chemically, they belong to the peraluminous Li-, Cs-, and Ta-bearing (LCT) family of pegmatites[18].

The Urmia Dokhtar Magmatic Arc (UDMA) is located on the eastern side of the Ghahavand Plain (Fig. 2). The UDMA on the eastern area of the Plain features Eocene volcanic and volcaniclastic rocks along with minor marine carbonate and evaporite deposits. These deposits have undergone deformation, resulting in the metamorphosis of marine carbonate and evaporate deposits that were uplifted and eroded[19]. The Eocene succession commences with a basal conglomerate and other coarse clastic rocks (Fig. 2), followed by a predominantly calc-alkaline volcanic series[20]. The intercalation of limestone and other evaporite deposits in this sequence suggests that the Eocene volcanism may have occurred in proximity to a marine environment[21]. The Oligomiocene units, known as the Qom Formation, are exposed in the northeastern part of the study area (Fig. 2).

Cretaceous sequences which include sandstone, shale, and limestone are observed around the Ghahavand Plain (Fig. 2). Three aspects have been identified as the primary causes of the desertification in the Ghahavand area[13]: (1) the creation of a regional plain in the Ghahavand area; (2) the multiple input streams to the field and the changing direction of the main river; and (3) the existing geological formation and geomorphological processes that produce fine-grained sediments in the central plain.

The plain is characterized by sedimentary rocks that have been transported and deposited by rivers over time. A significant expanse of clay-covered flats lies in the Ghahavand Plain (Fig. 3a-f), which is predominantly unsuitable for agricultural purposes. In certain regions, small patches of salt are discernible on the clay surface. These salt deposits in the study area are believed to have originated from the evaporation of water resulting from floods (Fig. 3e), which subsequently left behind a crust of salt. Beneath the sedimentary layers, there is a significant presence of limestone bedrock. This limestone is highly porous and has numerous joints and fractures. Mud cracks, also known as desiccation cracks, form when muddy sediment dries and contracts (Fig. 3c). These cracks are typically polygonal and can provide valuable information about past environmental conditions. In the Ghahavand Plain, mud cracks are indicative of periods of drying and wetting cycles, which are influenced by climatic conditions.

Sample collection

Thirty surface sediment samples were collected from Ghahavand Plain during the spring of 2023, focusing on the uppermost layers. The sampling sites were carefully selected to represent the major lithological unit of the area. The sampling location is depicted in Fig. 2. To ensure consistency and comparability across the dataset, all samples were collected at a uniform depth of 20 cm below the ground surface. This standardized depth was chosen based on preliminary field assessments, which indicated that the top 20 cm of sediment is most representative of recent depositional processes. Although the sediment types a bit varied between sites, the sampling depth remained constant to minimize variability related to vertical stratification and to enhance the representativeness of the surface sediment composition across the plain. Immediately after collection, each sample was sealed in a plastic bag to prevent moisture loss and chemical alteration, thus preserving the in-situ characteristics of the sediments for subsequent laboratory analysis (Fig. 3f). All collected surface sediment samples were visually inspected and described during fieldwork. The majority of the samples consisted of fine-grained sediments with a light brown coloration, indicative of their recent depositional nature.

Methods

Samples were naturally dried in the laboratory at the University of Kurdistan, Sanandaj, Iran. The thirty sediment samples from the Ghahavand Plain were used for chemical analysis. Each sample, approximately 500 g of each sediment sample, was pulverized using an agate motor to a fineness of 250 mesh. These powdered samples were then used for quantitative analysis of major and trace elements, Sr isotope analysis, and mineral composition analysis.

Mineral compositions

Four sediment samples were selected for mineral analysis. The analysis was conducted using an X-ray diffractometer (XRD) at the Institute for Space–Earth Environmental Research (ISEE), Nagoya University, Japan. The samples were flattened onto a slide and prepared into a 1 cm × 1 cm film for analysis. To identify the mineral composition of the entire sediment sample, MiniFelx (Rigaku) was used with a Cu-K source, a 2θ range of 5° to 80°, and four-hour runs. The instrument's built-in software, Match, was employed to detect mineral species and estimate their relative percentage.

Chemical composition and Sr isotopic composition

For quantitative analysis of Major elements, 0.5 g of each rock powder was combined with 5 g of Lithium tetraborate and melted at 1200 °C to form a glass bead. Subsequently, the major elements were analyzed using wavelength dispersive X-ray fluorescence spectrometry (WD-XRF), a Rigaku ZSX Primus II, at Nagoya University in Japan. Approximately 0.5 g of each sample were weighed and heated to 950 °C for three hours to assess the loss on ignition (LOI).

To analyze trace elements, including rare earth elements (REE), 100 mg of each rock powder sample was digested in a covered PTFE beaker. The digestion process involved 3 ml of 38% hydrofluoric acid (HF) and 0.5–1 ml of 70% perchloric acid ($HClO_4$). The sample was left on the hot plate for 72 h. Following the digestion process, the samples were dried and dissolved in concentrated nitric acid (HNO_3) acid. After drying, they were dissolved in approximately 10 ml of 6 M distilled hydrochloric acid (HCl). The resulting solution was then divided into two aliquots. One aliquot was used for quantitative analysis of trace elements, including REE, while the other was used for the isotope analysis of strontium (Sr). The first aliquot was dried and subsequently dissolved in 2% nitric acid (HNO_3) for inductively coupled plasma mass spectrometry (ICP-MS) analysis. The
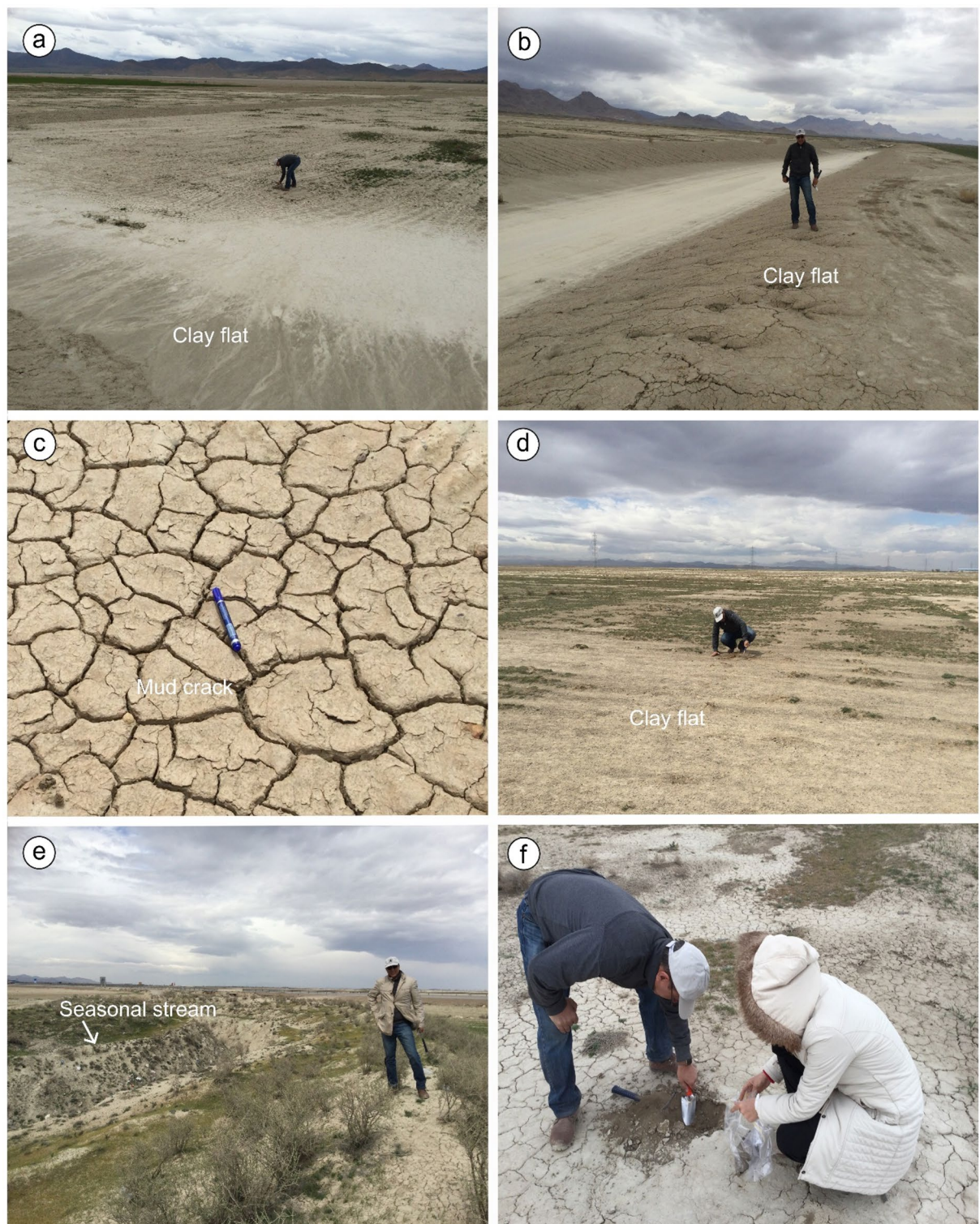
Fig. 3. (**a-f**) Photographs of field observation of the clay flat of the Ghahavand Plain. Mud cracks are commonly observed in the Ghahavand Plain. The image belongs to the authors. These photographs were taken by the authors (HA and ND) during their fieldwork.

trace elements were analyzed using ICP-MS Agilent 7700x at Nagoya University in Japan, and the analytical errors are below 5%. The second aliquot underwent conventional column chemistry to isolate the Sr portion.

The Sr isotope ratios were determined using GVI IsoProbe-T thermal ionization mass spectrometer (TIMS) at Nagoya University in Japan. NIST SRM 987 was employed as the standard for natural Sr. The standard value obtained in this study was 0.710278 ± 0.000009 ($n = 4$, 2 SD).

Results
Mineral composition
The major properties of four sediment samples from the Ghahavand Plain were as follows (Fig. 4). Quartz is the most common silicate mineral, followed by gyrolite, a rare calcium silicate hydrate mineral associated with volcanic or metamorphic rocks. Calcite is the most abundant carbonate mineral (Fig. 4a-d). The samples also contain small amounts of dickite (LFM-2 and LFM-13, Fig. 4a, d) and kaolinite (LFM-13, Fig. 4c). Natrolite is present in low amounts (LFM-20, Fig. 4d). The lithium-bearing mineral zabuyelite (LFM-13, Fig. 4c) is also
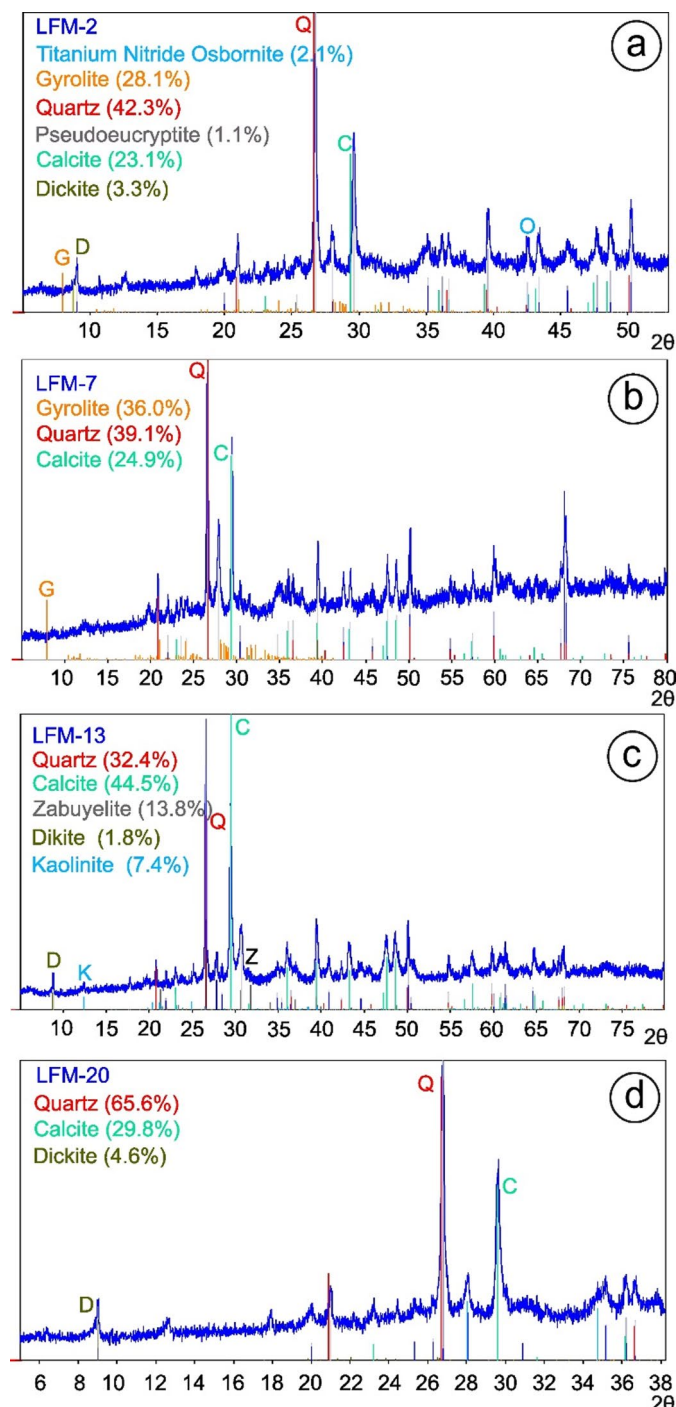

Fig. 4. X-ray diffractograms of representative sediment samples of the Ghahavand Plain. (**a**) Titanium nitride osbornite, gylorite, quartz, psedoecryptite, calcite, and dickite in the LMF-2 sample. (**b**) Gylorite, quartz, and calcite in the LFM-7 sample. (**c**) Gylorite, quartz, calcite, zabuyelite, dikite, and kaolinite in the LMF-13 sample. (**d**) Quartz, calcite, and natrolite in the LMF-20 sample. The percentages in each sample refer to the intensity of diffraction peaks relative to the highest peak in the sample.

present and is an important natural industrial chemical for lithium carbonate production. Zabuyelite forms under specific evaporitic conditions, and its discovery provides valuable insights into the geochemical process of lithium in the salt lake environment[22]. Additionally, a small amount of psedoeucrptite is present (LFM-2, Fig. 4a), which is a rare lithium aluminum silicate mineral related to lithium-rich pegmatite.

Major and trace element compositions

The Major oxide composition of 8 sediment samples of the Ghahavand area is given in Supplementary Table S1. The LOI is high and ranges from 10.0 to 21.9 wt%, containing volatile components such as crystalline water in gyrolite mineral, inorganic carbon (CO_2) in carbonate minerals, and hydroxyl in clay minerals. The SiO_2 content ranges from 42.3 to 56.8 wt% with an average of 48.5 wt%. The Al_2O_3 content varies between 6.70 and 14.7 wt% (average 11.5 wt%). The Fe_2O_3 content spans from 2.86 to 6.39 wt% with an average of 5.13 wt%. The MnO content varies between 0.063 and 0.122 wt% (average 0.099 wt%). The CaO content ranges from 7.71 to 22.3 wt% with an average of 12.7 wt%. The MgO content spans from 2.49 to 4.63 wt% (average 3.53 wt%). The Na_2O content ranges from 0.92 to 3.19 wt% with an average of 1.73 wt%, and the K_2O content ranges from 0.99 to 2.68 wt% with an average of 2.07 wt%. The Ghahavand Plain sediments are characterized by low contents of TiO_2 (0.57–0.79 wt%, average 0.68 wt%) and P_2O_5 (0.12–0.25 wt%, average 0.18 wt%).

The composition of trace elements, including rare earth elements (REE), in the Ghahavand Plain sediments is presented in Supplementary Table S2. The Li concentration ranges from 30.3 ppm to 102 ppm with an average of 55.1 ppm. The Rb content varies from 32.2 ppm to 109 ppm, averaging 71.1 ppm. The Cs concentration ranges from 2.19 ppm to 8.06, averaging 5.11. The Sr content varies from 271 ppm to 10,900 ppm, averaging 972 ppm. The Ba concentration ranges from 162 ppm to 463 ppm with an average of 311 ppm. The Zr content ranges from 37.0 ppm to 127 ppm with an average of 78.0 ppm. The Pb content ranges from 7.74 ppm to 33.5 ppm with an average of 18.5 ppm. The Th and U contents range from 3.43 ppm to 12.2 ppm (average 7.83 ppm) and 1.43 ppm to 3.02 ppm (average 1.91 ppm), respectively. The Zn value varies from 36.5 ppm to 98.5 ppm with an average of 77.2 ppm. The Cu content ranges from 11.6 ppm to 32.9 ppm, averaging 25.2 ppm. The V content ranges from 40.1 ppm to 132 ppm with an average of 93.2 ppm. The Cr value ranges from 43.5 ppm to 113 ppm, averaging 83.0 ppm. The Co and Ni contents range from 6.18 ppm to 18.5 ppm (average 13.6 ppm) and 29.2 ppm to 83.8 ppm (average 60.9 ppm), respectively.

The concentrations of the trace elements are normalized to those of the upper continental crust (UCC)[23] (Fig. 5a). Most trace elements (Y, Zr, Nb, Ba, La, Ce, Nd, Sm, Yb, Lu, Pb and Th) in the sediments have lower concentrations than in the UCC. However, Sr and Cs in the sediments, except for four samples, are found in higher concentrations than in the UCC (Fig. 5a).

The total concentration of rare earth elements (REE) ranges from 68.3 ppm to 179 ppm, with an average of 134 ppm. The light REE (LREE) content varies between 55.6 ppm and 147 ppm, averaging 107 ppm, while the heavy REE (HREE) content ranges from 5.47 ppm to 14.4 ppm, with an average of 11.5 ppm (Supplementary Table S2). Chondrite-normalized REE pattern[24] is shown in Fig. 5b. The Eu and Ce anomalies, Eu/Eu* and Ce/Ce*, are calculated using the following formulas: $Eu/Eu^*=2\times Eu_{CN}/(Sm_{CN}+Gd_{CN})$ and $Ce/Ce^*=2\times Ce_{CN}/(La_{CN}+Pr_{CN})$ (Supplementary Table S2). The normalized ratios of $(La/Yb)_{CN}$, $(La/Sm)_{CN}$, and $(Gd/Yb)_{CN}$ are also present in Supplementary Table S2. All samples show enrichment of LREE compared to HREE (Fig. 5b). The LREE/HREE ratio varies from 6.78 to 13.2 with an average of 9.38 (Supplementary Table S2). The $(La/Yb)_{CN}$ ratio ranges from 7.12 to 17.0, averaging 10.9, illustrating the significant fractionation between LREE and HREE. The $(La/Sm)_{CN}$ ratio, which indicates the LREE fractionation, ranges from 3.14 to 4.21 with an average of 3.65 (Supplementary Table S2). The $(Gd/Yb)_{CN}$ ratio, reflecting the HREE fractionation, ranges from 1.55 to 2.41, with an average of 1.95 (Supplementary Table S2). All samples show V-shaped patterns at Eu, negative Eu anomalies (Fig. 5b). The Eu/Eu* value ranges from 0.64 to 0.77, averaging 0.68. The Ce/Ce* value ranges from 0.93 to 1.02, with an average of 0.99.

The uniform REE pattern suggests that these sedimentary particles from the Ghahavand Plain may have originated from the same place.

Statistical analysis

This section focuses on the analysis of a substantial dataset to pinpoint lithium anomalies and their relationship with other elements. We have also applied general statistics commonly used in trace element exploration.

Stepwise factor analysis

Stepwise factor analysis (SFA), a specialized method within factor analysis, is used to identify multi-element associations within a geochemical dataset by progressively identifying noisy (non-indicator) elements and removing them from the analysis[25,26]. This process continues until a clear and significant multi-element signature is achieved[25,26]. The assumptions underlying factor analysis in geochemical contexts include the presence of linear relationships among variables, as well as the requirement that data distributions exhibit either normality or log-normality[27]. The normality tests Kolmogorov–Smirnov[28] is used. A significant Bartlett's test of sphericity ($p < 0.05$), and a Kaiser-Meyer-Olkin (KMO) measure ≥ 0.6 [30].

First, classical Principal Component Analysis (PCA) was used to extract the common factors. Then, the varimax method was applied for rotation, and factors with eigenvalues greater than 1 were retained for interpretation[29,30].

The SFA was used to extract factors, and the varimax rotation of factors was applied using the JASP software for our chemical data. Trace elements, except REE, were selected for SFA. The REE showed a high fraction and strong multicollinearity due to the uniform REE composition, they were omitted from the SFA.

Elements were classified into three main factors (Supplementary Table S3). In each step, elements less than 0.6 in any of the factors are eliminated. In the first step (F1), according to Supplementary Table S3a, Pb, Cd, and
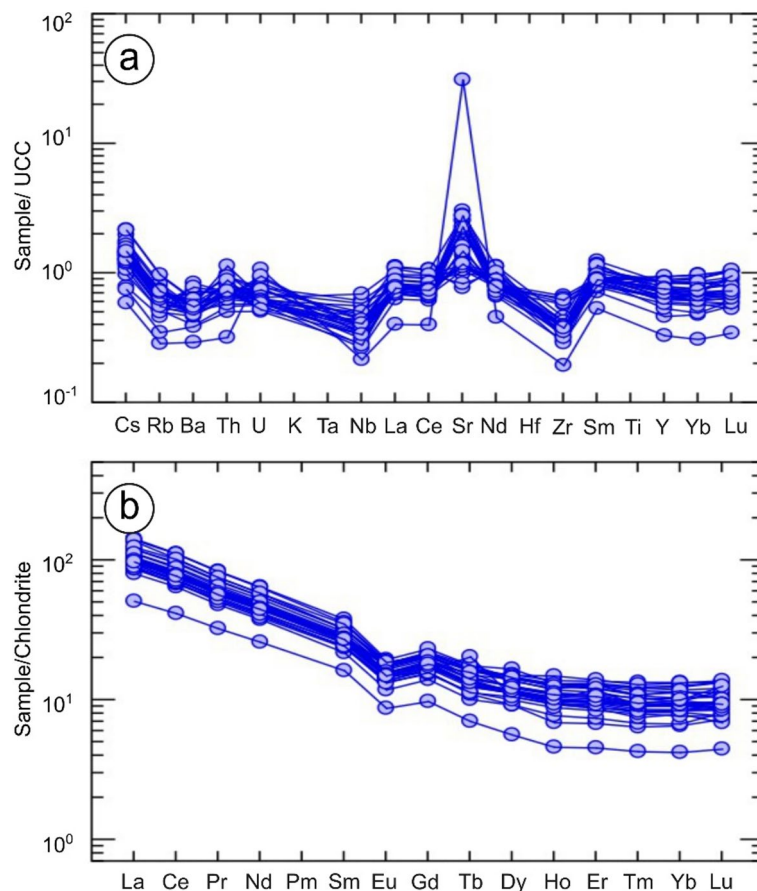
Fig. 5. (**a**) Upper continental crust (UCC) normalized patterns for the Ghahavand Plain sediments [27]. Most trace elements, such as Pb, Ba, Th, U, Nb, La, Ce, Nd, Zr, Sm, Y, Yb, and Lu, show lower concentrations than the UCC. However, Cs and Sr, except for four samples, show higher concentrations than the UCC. (**b**) Chondrite normalized REE patterns for the Ghahavand Plain sediments [28]. All samples show LREE enrichments and negative Eu anomalies.

Be were eliminated from the dataset. In the next step (F2), the factorization was performed on the remaining data, and this process was repeated three times until the elements were correctly assigned to the existing factors. On this account, in the second step (F2) (Supplementary Table S3b), Nb are eliminated, and the result of the third step (F3) is shown in Supplementary Table S3c.

The first factor in the third step (F1-3) show high coloration of Rb (0.94), Cr (0.93), Co (0.89), Ni (0.85), Cu (0.83), Cs (0.82), Ga (0.76), Sc (0.69), V (0.69) and Th (0.65). F3-2 show high load of Sc (0.70), V (0.63), Zn (0.80), Sb (0.88), Ba (0.97) and Zr (0.90) and the third factor in the third step (F3-3) includes Li (0.74), Sr (0.81), and U (0.67), suggesting a strong correlation among Li, Sr, and U.

Fractal analysis
The Concentration-Number (C-N) fractal method, used in geology, identifies geochemical anomalies by analyzing spatial data and concentration of elements and shows that there is a relationship between the frequency distribution of elemental concentrations and the cumulative number of samples[31,32].

A fractal model is generally expressed as follows[33]:

$$N(r) = C\,r^{-D} \tag{1}$$

where r denotes the characteristic scale, C is the scale factor, D is the fractal dimension, and N(r) represents the count or sum of occurrences where the scale factor is greater than or equal to r[33].

This method can be expressed as follows[34,35]:

$$N(\geq \rho) \propto F\rho^{-D} \tag{2}$$

where ρ represents the element concentration, N($\geq\rho$) represents the cumulative number of samples with corresponding concentrations, and different concentration intervals.

Based on the C-N log-log plot, the lithium (Li) concentrations in the study area can be categorized into seven distinct populations, each defined by specific thresholds (Fig. 6a). The first population is identified by a
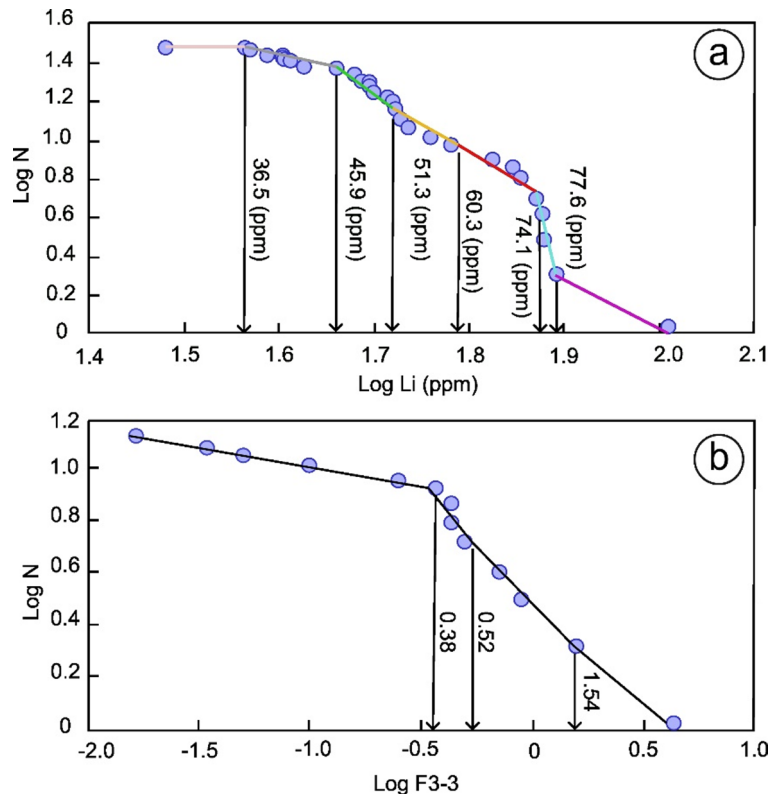
Fig. 6. (**a**) C-N log-log plot of Li for the Ghahavand Plain sediments, showing the seven populations. The first group is equal to or less than 39.5 ppm, the second is between 39.5 and 45.9 ppm. The third group is between 45.9 and 51.3 ppm. The fourth group is 51.3 to 60.3 ppm. The fifth group is 60.3 to 74.1 ppm. The sixth group is 74.1 to 77.6, and the last group is higher than 77.6 ppm. (**b**) C-N log-log of F3-3 for the sediments, showing three thresholds at 0.38, 0.52, and 1.54.

threshold of 36.5 ppm, representing the lowest concentration range. The second population begins at 45.9 ppm, with Li concentration ranging from 36.5 ppm to 45.9 ppm. The third population is defined by a threshold of 51.3 ppm. The fourth population indicates a further rise in the level of Lithium. The fifth population starts at 74.1 ppm, while the sixth population ranges from 74.1 ppm to 77.6 ppm. Finally, the seventh population includes Li concentrations equal to or greater than 77.6 ppm, representing the highest concentration range observed in the study area. The C-N log-log plot (Fig. 6a) provides a clear depiction of the distribution and segmentation of Li concentrations across the region. These populations are shown in Fig. 7 using Arc-GIS Pro, and the sediment samples with the higher Li concentrations appear in the northern part of the study area.

Herein, the C-N fractal is used for factor scores. In this step, the log-transformed data were grouped by stepwise factor analysis, focusing on factor 3 in the 3rd step (F3-3). This includes categories of less than 0.38, between 0.38 and 0.52, from 0.52 to 1.54, and greater than 1.54 (Fig. 6b). The sediment samples with higher Li, Sr, and U appear in the northern section of the study area, as illustrated in Fig. 8.

Sr isotopic composition

Supplementary Table S4 presents the $^{87}Sr/^{86}Sr$ ratios from eight sediment samples in the Ghahavand area. The ratio ranges from 0.7078 to 0.7103 with an average of 0.7092. The variation in the Sr isotope ratio is minimal, thereby suggesting a consistent source for the sediments and their connection to the surrounding rocks. This will be further explored in the discussion.

Discussion

Fine-grained sediments, like clays, often exhibit higher Li concentrations due to their greater surface area and ability to adsorb Li ions[36]. Additionally, Li tends to accumulate in sediments rich in lithium-bearing minerals, such as clays, which are common in certain geological settings[11].

The presence of lithium in clay flats is influenced by the interplay of the weathering intensity and the composition of source sediments. Warm and humid paleoclimates often drive intense chemical weathering, which enhances the leaching of Li from primary minerals and its incorporation into secondary clay minerals like smectite and illite[37]. The mineralogy and Li content of the source sediments are also crucial, as Li-rich parent rocks such as granites or volcanic deposits provide higher initial Li concentrations[38]. Over time, chemical weathering causes Li to be liberated from its sources and accumulated in clay flats. Investigation of the chemistry of these sediments makes them valuable records for reconstructing past weathering conditions and climatic
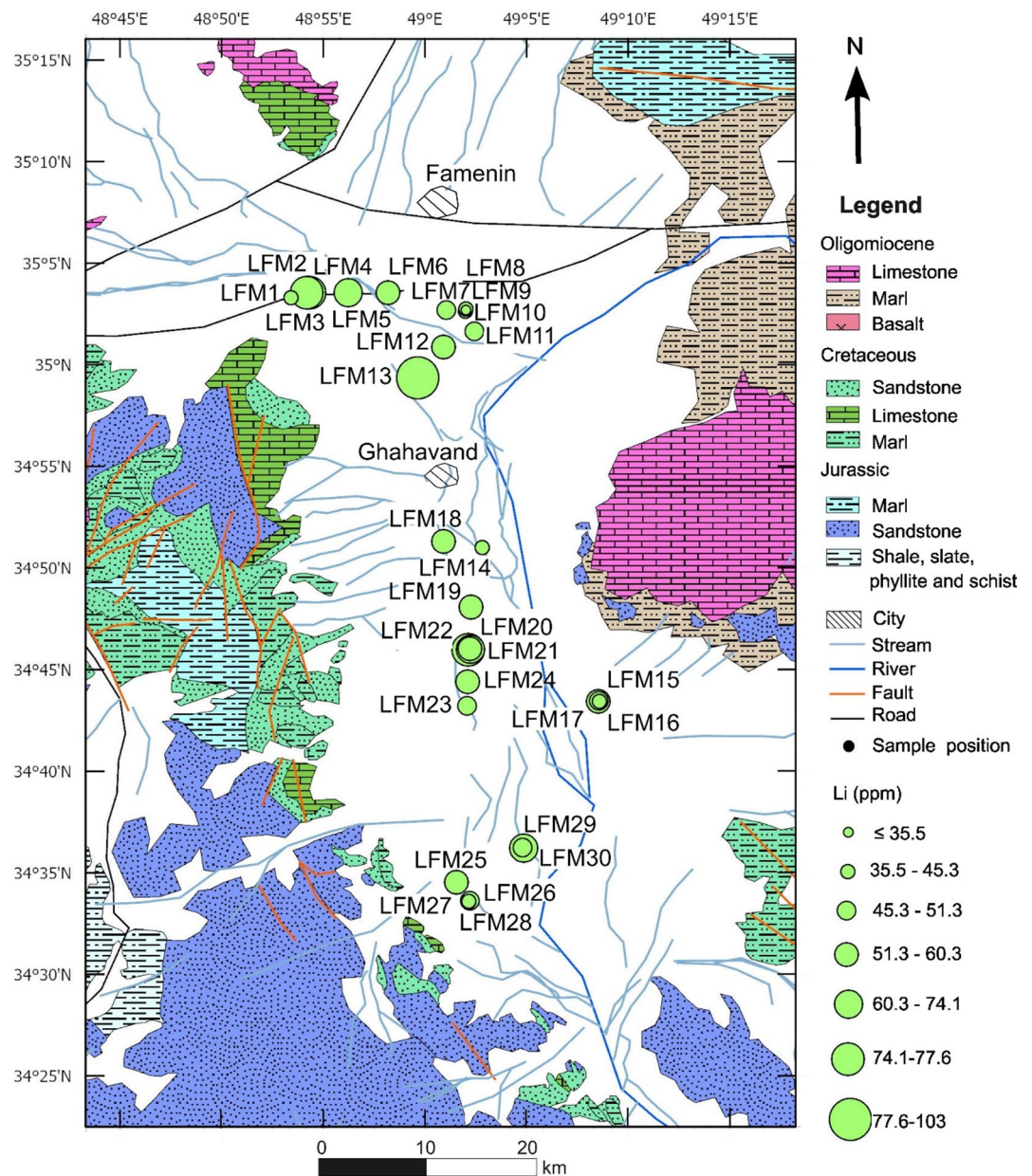
Fig. 7. Seven populations of Li concentration based on the C-N fractal model on the geological Map, using ArcGIS Pro online for windows version 3.5.2 (https://www.arcgis.com) and Inkscape for Mac version 1.3.2 (http://Inkscape.en.softonic.com). The main anomaly in Li concentration occurs mostly in the northern part of the study area.

histories[39]. Herein, we discuss the Li distribution and its relationship to the paleoenvironment of the Ghahavand Plain, because weathering plays a crucial role in the mobilization, redistribution, and concentration of Li within geological systems. In arid regions, lithium concentrations through evaporation processes, particularly in playas and flats, where evaporative enrichment occurs, lead to the accumulation of lithium.

Lithium-bearing minerals in the ghahavand plain sediments

The mineral composition of the sediment samples from the Ghahavand Plain highlights promising prospects for lithium resources, particularly due to the presence of lithium-bearing minerals. The most significant finding is the identification of zabuyelite (Li_2CO_3) in the sample LFM-13 (Fig. 4c). Evaporate concentration of lithium leads to the formation of lithium minerals such as lithium carbonate (Li_2CO_3)[11]. Zabuyelite is a critical natural source of lithium carbonate, and is a key industrial chemical that is utilized extensively in the production of lithium-ion batteries, ceramics, glass, and other high-tech applications. Its presence in substantial amounts suggests the potential for economic extraction and utilization of lithium from this region. Additionally, the detection of pseudoeucryptite, a rare lithium aluminum silicate mineral (LFM-2, Fig. 4a), further supports the
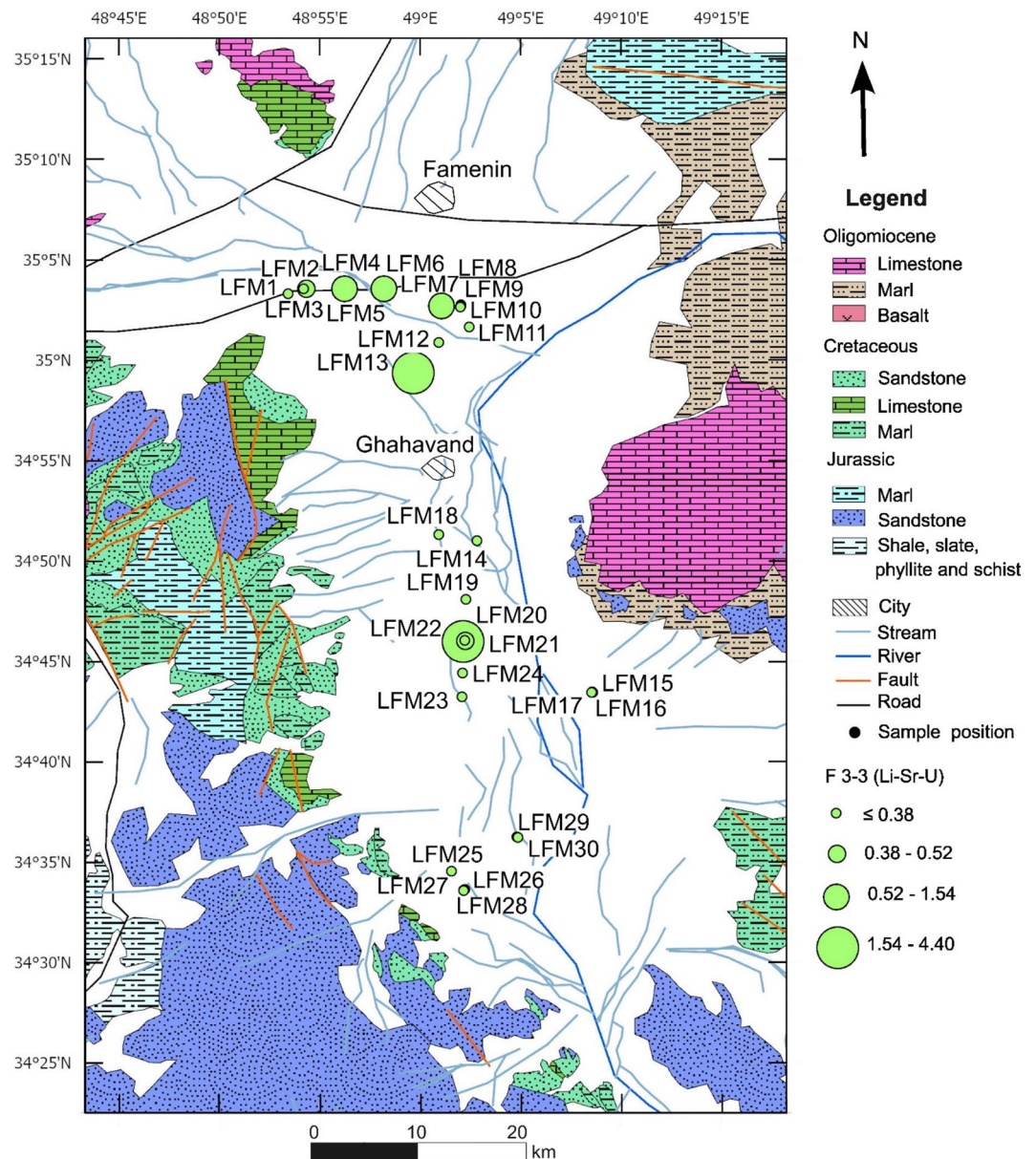
Fig. 8. Distribution map of F3-3 (Li-Sr-U) based on C-N fractal mode for the Ghahavand Plain sediments. This figure was created using ArcGIS Pro online for the Windows version 3.5.2 (https://www.arcgis.com) and Inkscape for Mac version 1.3.2 (http://Inkscape.en.softonic.com). The main anomaly for F3-3 mostly occurs in the northern part of the study area.

lithium prospect, as it is typically associated with lithium-rich pegmatites. Small amounts of lithium carbonate (zabuyelite) and lithium aluminum silicate (pseudoeucryptite) are also observed. The presence of these minerals indicates that the Ghahavand Plain may host lithium-enriched geological formations, which could be explored further for resource development.

The coexistence of other silicate and carbonate minerals, such as quartz, gyrolite, and calcite (Fig. 4), provides further context for understanding the geological environment and the processes that may have concentrated lithium-bearing minerals in this area. For example, gyrolite is hydrous calcium, often found in association with zeolite in volcanic cavities or hydrothermal environments. Overall, the mineralogical findings underscore the potential of the Ghahavand Plain as a prospective site for lithium exploration and extraction.

Chemical composition and clay-type lithium resources

The sediments in the Ghahavand area exhibit a diverse geochemical composition, primarily characterized by varying concentrations of SiO_2, Al_2O_3, Fe_2O_3, CaO, and MgO. The contents of SiO_2 and Al_2O_3 range from 42.3 to 56.8 wt% (average 48.5 wt%) and from 6.70 to 14.7 wt% (average 11.5 wt%), respectively. These indicate a significant presence of silicate minerals. The Fe_2O_3 content ranges from 2.86 to 6.39 wt% (average 5.13 wt%).

Notably, the CaO content, ranging from 7.71 to 22.3 wt% (average 12.7 wt%), highlights a substantial carbonate component, while low MgO levels (2.49–4.63 wt%, average 3.53 wt%) are evident. Based on these characteristics, the Ghahavand Plain sediments can be classified as carbonate-rich clay sediment.

Clay-type lithium resources could be divided into three categories: volcanic type, carbonate type, and jadarite type[11,40,41]. Volcanic clay-type lithium resources are formed through volcanic eruptions. The main lithium-bearing minerals found in volcanic clay-type lithium resources are illite and smectite. The lithium is incorporated within their crystal lattice structures. In addition, these resources are rich in SiO_2 and magnesium (Mg), typically with concentrations exceeding 50% for SiO_2 and 10% for Mg, respectively[7,42,43]. Lithium resources of the carbonate type are formed through the weathering and deposition of carbonate rocks[43]. As these rocks break down into clay, lithium becomes concentrated, leading to the formation of clay-type lithium deposits. The primary lithium-bearing minerals in carbonate-type lithium resources are clay minerals such as montmorillonite, kaolinite, and others. The lithium is typically adsorbed within the layered structures of these minerals. The carbonate type of lithium deposit is primarily characterized by its elevated concentrations of SiO_2 and Al_2O_3, accompanied by high Ca concentrations and comparatively low Mg concentrations[44]. The main lithium-bearing mineral in jadarite-type lithium deposits is jadarite itself. This unique mineral contains both lithium and boron, and its chemical formula is $LiNaSiB_5O_7(OH)$. It is characterized by a Li_2O content of 7.3% and a B_2O_3 content of 47.2%. Although jadarite also contains a significant amount of SiO_2, it is distinguished by its high Na content. Additionally, jadarite has a negligible Mg content, which is advantageous for the extraction of lithium[11,41].

We compare the Ghahavand Plain sediments with the three types of lithium host deposits across various regions. The Ghahavand Plain sediments show moderate levels of SiO_2, Al_2O_3 and MgO and high level of CaO (42.3–56.8 wt%, 6.70–14.7 wt%, 2.49–4.63 wt%, 7.71–22.3%, respectively) with a low presence of dickite. These characteristics are shared by both volcanic and carbonate clay types.

SFA and C-N fractal modeling

The first factor identified in step 3 (F3-1) exhibits high loadings for the elements Rb, Cr, Co, Ni, Cu, Cs, Ga, Sc, V, and Th, as presented in Supplementary Table S3c. Rb, Cs, Ga, and Th are typically in felsic rocks such as granites and pegmatite[45,46]. Cr, Co, Ni, Sc, and V are more characteristic of mafic or ultramafic rock[47] which likely reflects a mixed contribution from felsic and mafic/ultramafic rocks. The second factor show coloration of Sc (0.70), V (0.63), Zn (0.80), Sb (0.88), Ba (0.97), and Zr (0.90) (Supplementary Table S3c). Sc, V, and Zr are typically considered conservative, lithogenic elements, often linked to the detrital fraction derived from the weathering of mafic/intermediate igneous rocks[48]. Zn, Ba and Sb are relative to upper continental crust[48].

Results obtained by the SFA (Supplementary Table S3c) show that Li paragenesis is Sr and U (F3-3). The C-N log-log plot in the study area shows seven distinct populations (Fig. 6a). The highest concentration level in this study area is 77.6 ppm or higher and is observed in the northern part of the Ghahavand area (Fig. 7).

According to the results presented in Supplementary Table S3c, the paragenesis of Li is closely associated with Sr and U within the F3-3. Geochemical analysis using the C–N log-log plot reveals the presence of seven geochemically distinct populations within the study area (Fig. 6a), suggesting diverse Lithological or hydrothermal influences. The highest recorded Li concentration, reaching 77.6 ppm or greater, is predominantly located in the northern sector of the Ghahavand area (Fig. 7), indicating a potential geochemical anomaly or mineralization hotspot in that region.

In addition, the C-N fractal distribution for F3-3 (Li-Sr-U) showed that these elements have high concentration in the northern part of the Ghahavand Plain. Lithium and Sr exhibit distinct behavior during the weathering process, which can provide valuable insight into geochemical cycles and the environment. Li is primarily hosted in silicate minerals, and during weathering, Li is released from minerals and can be transported by rivers[37]. Misra and Froelich[37] used the behavior of Sr and Li to get insights into physical weathering dynamics based on continental inputs. These elements are released from bedrock during weathering and eventually make their way into rivers. Additionally, Sr is released from both silicate and carbonate minerals during weathering. The uranium (U) content in the Ghahavand sediments ranges from 1.43 to 3.02 ppm. Generally, sediments in oxic environments have low U concentrations, while those in reducing environments—like continental margin sediments—typically have higher concentration of 1 to 10 ppm. The relatively low U content in the Ghahavand sediments suggests they were deposited in an oxic environment.

Source material

Source of sediment based on chemical composition

The source of sediments can be determined by using various discriminant diagrams based on major and trace elements[49–51]. The DF1 and DF2 discriminant diagrams are based on the content of Major oxides in 248 groups of sandstone and mudstone. These diagrams categorize the source area into four provinces: mafic igneous, intermediate igneous, felsic igneous, and quartz sedimentary[52].

$$\text{Discrimination function 1 (DF1)} = 0.44TiO2 + 0.07Al2O3 - 0.25Fe2O3\,(\text{total}) - 1.142MgO \\ + 0.438CaO + 1.475Na2O + 1.426K2O - 6.861. \tag{3}$$

$$\text{Discrimination function 2 (DF2)} = -1.773TiO2 + 0.607Al2O3 + 0.76Fe2O3\,(\text{total}) - 1.5MgO \\ + 0.616CaO + 0.509Na2O - 1.224K2O - 9.09 \tag{4}$$

The major oxides are based on wt%. The calculated values indicate that DF1 and DF2 in the Ghahavand area have changed from −0.12 to 0.64 and from 1.67 to 2.90, respectively. This suggests that the sediment samples predominantly plot within the felsic volcano-plutonic field, which we acknowledge as the origin of these sediments (Fig. 9a).

Additionally, the low solubility of aluminum, titanium, and zirconium oxides and hydroxides in low-temperature aqueous solutions makes these elements effective tracers for sediment source discrimination. The Al_2O_3/TiO_2 ratio exceeding 21 indicates a felsic provenance, while those below 8 suggest a basic source rock[53]. The Al_2O_3/TiO_2 ratio in the Ghahavand sediment ranges from 11.8 to 19.7, with an average of 16.8, indicating
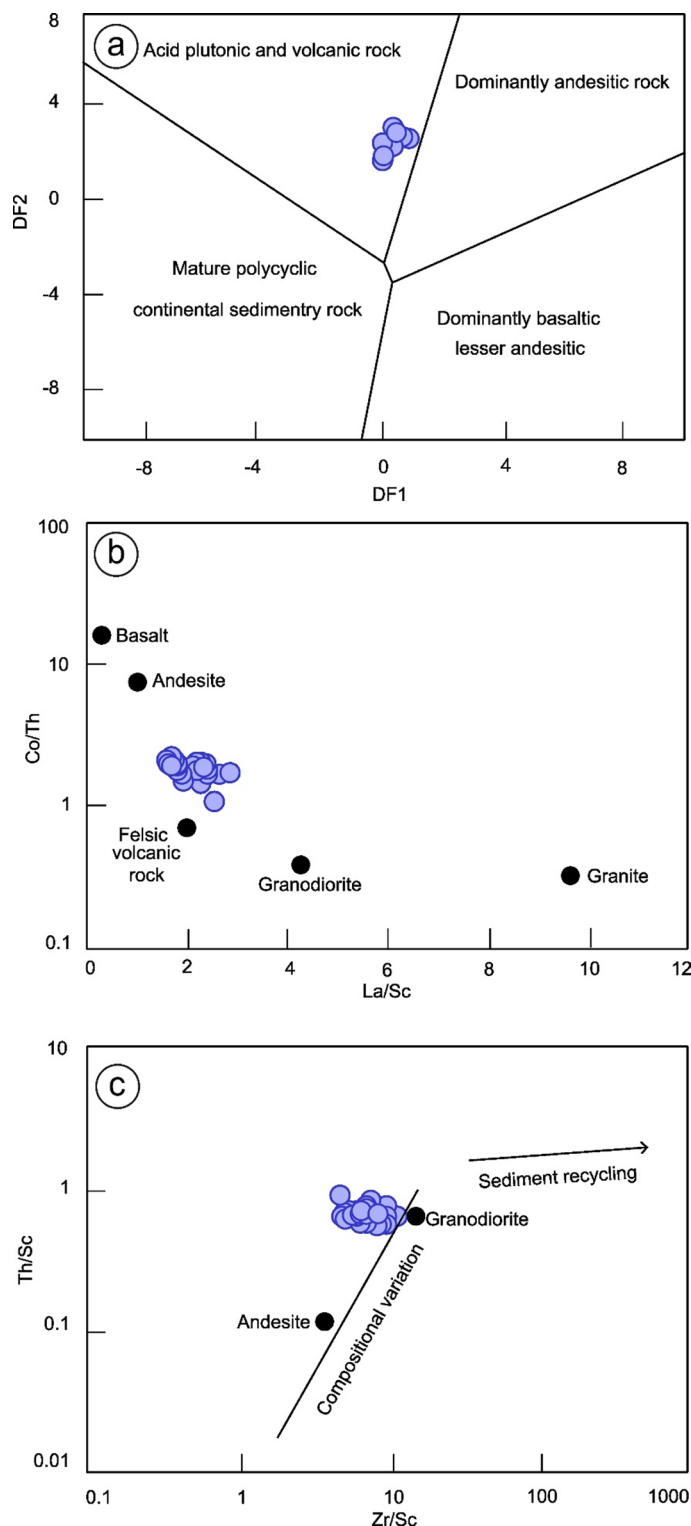

Fig. 9. (**a**) Discrimination diagram for the provenance of the Ghahavand Plain sediments [58]. Most of theGhahavand Plain sediments plot in the acid plutonic and volcanic rock. (**b**) La/Sc versus Co/Th diagram [60], showing the felsic volcanic rock for the source of the Ghahavand Plain sediments. (**c**) Zr/Sc versus Th/Sc diagram [63], indicating that the sediment source in the Ghahavand Plain is granodiorite.

a relatively high ratio (Supplementary Table S1). This suggests a stronger affinity to felsic rocks compared to mafic ones. Furthermore, trace elements such as Ti, Y, Th, Sc, Hf, and REE are essential for understanding the origin and composition of the source area because they are unlikely to migrate during the post-depositional process. Discrimination diagrams, such as La/Sc vs. Co/Th[54,55] show that the sediment in the Ghahavand area has a felsic rock affinity (Fig. 9b). Immobile elements such as Th, Sc, and Zr have brief residence times in water and are almost quantitatively transferred into the sediments[56]. On the Zr/Sc vs. Th/Sc diagram, the Ghahavand sediments are plotted in the domain of felsic igneous rock (Fig. 9c).

Source of sediment based on Sr isotopic composition

The $^{87}Sr/^{86}Sr$ ratio of the Ghahavand sediment ranges from 0.7078 to 0.7103 (Supplementary Table S4). Herein, the $^{87}Sr/^{86}Sr$ ratios of the Ghahavand sediments are compared to those of mantle and crustal source materials[57] modern seawater, marine carbonate, and the surrounding rocks (Fig. 10). The $^{87}Sr/^{86}Sr$ ratios of various granitoid types in the surrounding Alvand pluton are available in Shahbazi et al.[58]: the $^{87}Sr/^{86}Sr$ ratio of the gabbroic rock varies from 0.7020 to 0.7037, the aluminous porphyric granite shows high $^{87}Sr/^{86}Sr$ ratios, ranging from 0.7092 to 0.7194, the mylonitic granite shows high $^{87}Sr/^{86}Sr$ ratios of 0.7088, and the leucogranite has a $^{87}Sr/^{86}Sr$ range between 0.7127 and 0.7138 (Fig. 10). The $^{87}Sr/^{86}Sr$ ratio of the surrounding Eocene-Oligocene volcanic rock in the eastern Saveh ranges from 0.7046 to 0.7098[59] (Fig. 10). The $^{87}Sr/^{86}Sr$ ratio of Marine carbonate of Oligomiocene changes from 0.7078 to 0.7091[60]. The $^{87}Sr/^{86}Sr$ ratios of the sediments in the Ghahavand area are consistent with those of the aluminous porphyric granite and the mylonitic granite in the Alvand pluton, the Eocene-Oligocene volcanic rock in the eastern Saveh, and the Oligomiocene limestone.

Weathering and lithium concentration

Paleoclimate

Paleoclimate significantly impacts weathering processes, which subsequently affect lithium concentrations within geological systems. In periods of intense weathering, particularly in warm and humid paleoclimates, lithium can be leached from minerals and transported in water, accumulating in clays, brines, or evaporite deposits[11]. Conversely, arid paleoclimates can lead to increased evaporation, which concentrates lithium in closed basins, forming lithium-rich brine deposits of economic value[61]. It is imperative to comprehend the interplay between weathering and lithium concentration in paleoenvironments to identify conditions that favor lithium enrichment. This understanding is crucial for exploring this vital resource for renewable energy technologies.

To estimate the weathering condition in this area, geochemical proxies are employed to reconstruct paleoclimate conditions in the source areas[62,63]. Ga/Rb and Sr/Cu ratios in fine-grained sediments are commonly used as indicators to determine the paleoclimate[63,64]. Gallium (Ga) is predominantly associated with the fine-grained aluminosilicate fraction and is enriched in kaolinite-related deposits, which form in warm and humid climates[64,65]. Rubidium (Rb) is associated with illite, indicating that the region experiences weak chemical weathering due to dry and cold climatic conditions[64]. As the climate becomes colder and drier, the value of the Ga/Rb ratio in sediments decreases[64]. The Sr/Cu ratio, ranging from 1.3 to 5.0, is indicative of a humid environment, while those exceeding 5.0 indicate an arid environment[63,66,67]. Sediments typically exhibit high Ga/Rb and low Sr/Cu ratios in warm and humid climates[64,66].
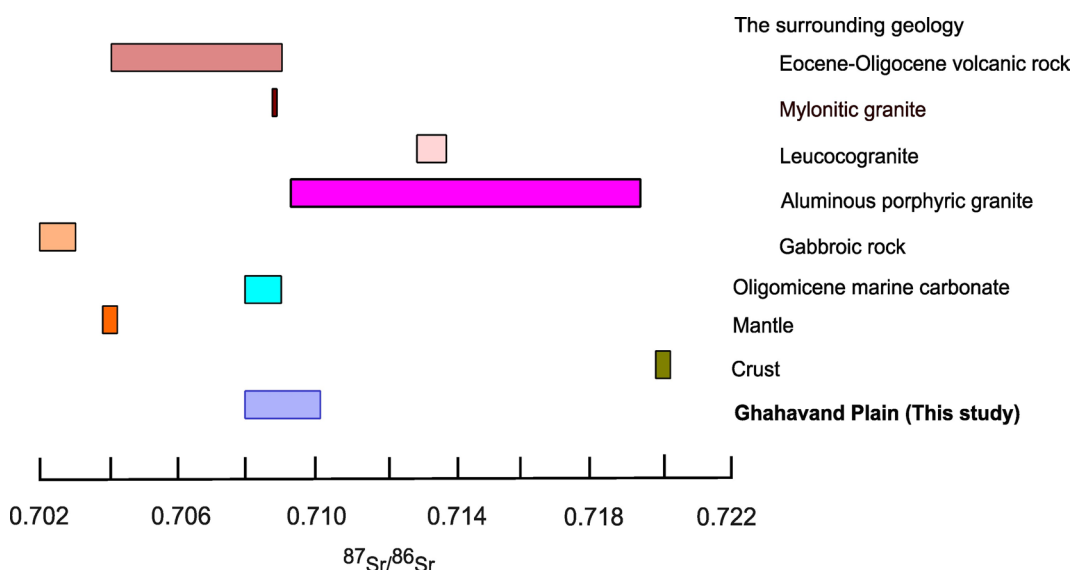

Fig. 10. Strontium isotope ratios of the Ghahavand Plain sediments and their potential sources: crust and mantle [64], the Oligomicene carbonate [67], the Alvand pluton [65] (gabbroic rock, aluminous porphyric granite, mylonitic granite, leucogranite), and the Eocene-Oligocene volcanic rock in the eastern Saveh [66].

The Ga/Rb ratio in the Ghahavand area ranges from 0.18 to 0.27, while the Sr/Cu ratio varies between 8.9 and 710. In the diagram (Fig. 11a), the sediment plots are situated along the boundary between the cool and warm arid domains with a greater affinity towards the cool domain.

Arid climate is characterized by minimal precipitation and are essential for natural process that concentrated lithium both in the brine and sedimentary deposits[68]In such regions, the combination of limited water flow and high evaporation rates during warmer periods contributes to the accumulation of lithium in closed basins, such as saline lakes, playas, and salt flats[69]. These environments are often referred to as host lithium-rich brines, where the concentration of elements increases as the water evaporates[70]. Notable examples include Li-rich salt flats such as the Salar de Atacama in Chile and the Salar de Uyuni in Bolivia, both of which are located in cold, arid regions[71].
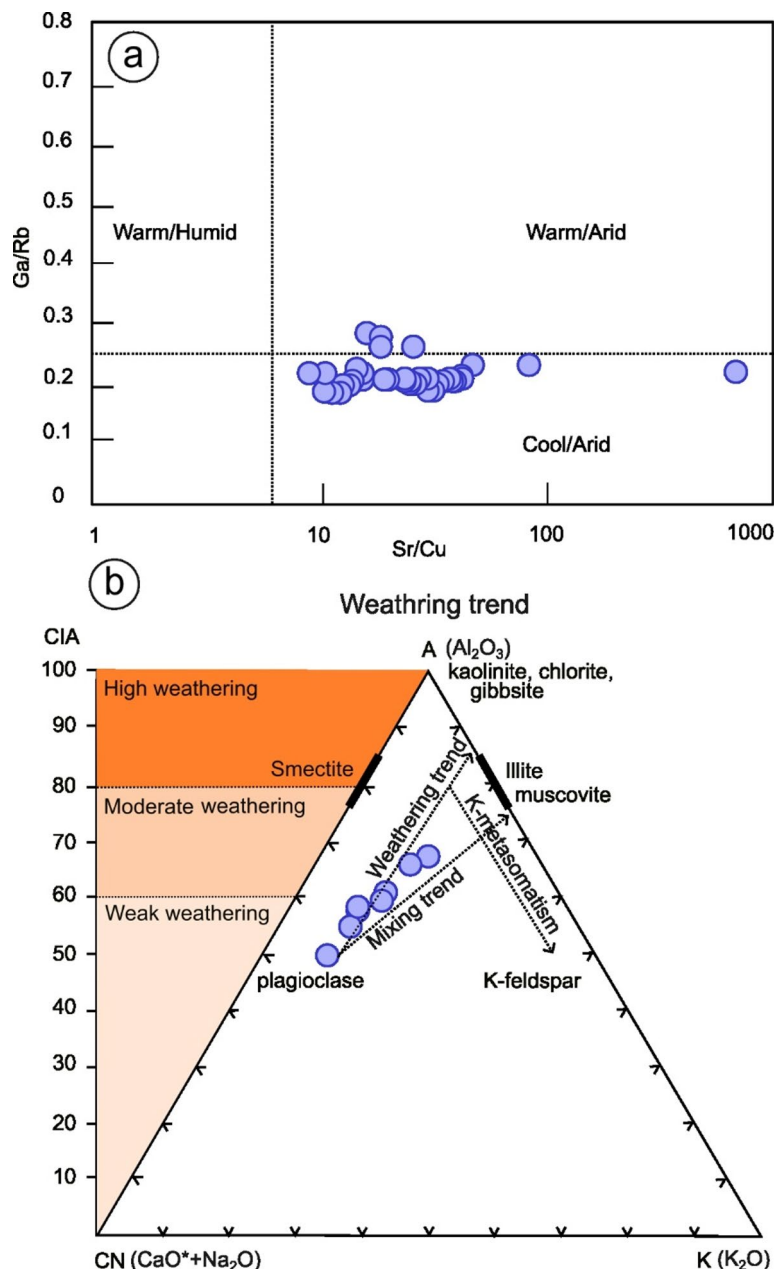

Fig. 11. (a) Plot of Sr/Cu versus Ga/Rb [70,73], of the Ghahavand Plain sediments, showing that the sediments were deposited under cold-dry conditions. (b) Diagram of A-CN-K [79,80]. Most of the Ghahavand Plain sediment samples plot above the plagioclase–K-feldspar line, showing weak to intermediate weathering (weathering line and mixing sediment linr from Srivastava et al.,[81] and K-metasomism line from Fang et al., [82]).

Weathering intensity based on CIA and PIA environmental factors

The chemical weathering of silicate rock in the source region exerts a substantial influence on the major element geochemistry of fine-grained siliciclastic sediments[72].

A reliable way to estimate the extent of weathering is to calculate the Chemical Index of Alteration (CIA) using molecular properties[72]:

$$CIA = [Al2O3/(Al2O3 + CaO* + Na2O + K2O)] \times 100 \qquad (5)$$

The CaO* was adopted based on the equation [$CaO_{residual}$ = molar CaO – molar $P_2O_5 \times 10/3$][54] when CaO residual is less than Na_2O content, then the CaO* is equal to $CaO_{redisual}$ if $CaO_{redisual}$ is greater than Na_2O, then CaO* is replaced by the Na_2O value[54].

The index values are 50 for unaltered albite, anorthite, and potassic feldspar, whereas the value for diopside is 0 [76]. Consequently, fresh basalt has values ranging from 30 to 45. Granite and granodiorite, on the other hand, have higher values, ranging from 45 to 55. Muscovite has a value of 75, while illite, montmorillonite, and beidellite range from 75 to 85. Kaolinite and chlorite have the highest values, close to 100. Therefore, the average shale has values ranging from 70 to 75, attributable to its substantial clay mineral content[72].

The CIA value in the Ghahavand sediments ranges from 50.3 to 67.9 (Supplementary Table S1) with an average of 59.7 (Fig. 11b). Bai et al.[73] suggested that CIA values between 50 and 65 reflect a cold-dry climate with reduced chemical weathering. When the CIA is between 65 and 85, it is indicative of a warm-humid climate with moderate chemical weathering. And, when the CIA is between 85 and 100, it reflects a hot and humid paleoclimate with strong chemical weathering. The weathering trend can be illustrated on Al_2O_3-($CaO*+Na_2O$)-K_2O (A-CN-K) triangular plot[74,75] (Fig. 11b). The diagram thus tracks the progressive breakdown of unstable minerals and the enrichment of stable ones, providing insight into the degree of weathering and sediment maturity. In the ternary A-CN-K diagram[75] most of the Ghahavand sediment samples plotted above the plagioclase–K-felspar line. In the A-CN-K diagram, some data exhibit a slight deviation from the typical weathering trend, displaying a pattern parallel to the A-CN line and indicating a mixing trend[76] (Fig. 11b). Furthermore, no samples demonstrate evidence of K-metasomatism trend[77] within the A-CN-K trend (Fig. 11b). If K-metasomatism occurs in sediments during diagenesis, it will increase the potassium content in the sedimentary rocks, which in turn results in a lower CIA value[77].

The intensity of source weathering can also be estimated using the related plagioclase index alteration (PIA) as follows[78]:

$$PIA = (Al2O3 - K2O)/(Al2O3 + CaO* + Na2O - K2O) \times 100 \qquad (6)$$

This quantifies the degree of destruction of plagioclase. The PIA value of unweathered plagioclase is 50, and the PIA value of completely altered Material is 100. The PIA value in the Ghahavand sediment ranges from 50.4 to 75.8, with an average of 63.0 (Supplementary Table S1), indicating less to moderate alteration of plagioclase in the sediments.

Lithium is a mobile element and tends to leach out of minerals over time. In the process of intermediate weathering, primary minerals such as feldspar and pyroxene begin to experience a phase transformation that involves the release of lithium. However, the extent of leaching observed in the Ghahavand sediments (PIA = 50.4–75.8) is less pronounced when compared to sediments in highly weathered environments (PIA ~ 100). As a result, lithium concentrations remain moderate, often accumulating in secondary minerals or being transported by water before stabilizing in advanced weathering profiles[79].

Depositional environment

The ratios of trace elements U/Th and V/Cr are highly effective indicators of the oxidation-reduction conditions within sedimentary environments[80,81]. When the U/Th ratio in sediments is below 0.75 and the V/Cr ratio is less than 2.0, it suggests an oxic environment[82]. Conversely, values exceeding 1.25 for U/Th and 4.25 for V/Cr indicate a reducing environment. The U/Th ratio in the sediment of the Ghahavand area ranges from 0.15 to 0.37, except one sample (0.88), and the V/Cr ratio ranges from 0.85 to 1.98, with an average of 1.16 (Supplementary Table S2), suggesting an oxic environment (Fig. 12a, b).

The concentrations of V and Ni in fine-grained sediments are sensitive to the redox conditions of the water column and can serve as indicators to assess the depositional conditions[83,84]. The ratio of V/(V + Ni) effectively reflects sedimentary redox conditions[80]: Values greater than 0.77 indicate relatively reducing environments, while those below 0.60 suggest relatively oxidizing settings; intermediate values denote weakly oxidizing environments[80]. The obtained V/(V + Ni) ratio in the sediment of the Ghahavand Plain ranges from 0.53 to 0.76, with an average of 0.61 (Supplementary Table S2), suggesting that the sediment was formed in a weakly oxic environment (Fig. 12c).

Additionally, the cerium anomaly (Ce/Ce*) serves as a valuable geochemical proxy for redox conditions. The solubility of Ce^{3+} is much higher than that of Ce^{4+}, and cerium present as Ce^{3+} in rock-forming minerals will be readily converted into Ce^{4+} in oxic water, resulting in positive or negative Ce anomalies (e.g., van der Weijden and van der Weijden [89]) The Ce/Ce* values of the Ghahavand sediments range from 0.94 to 1.02, with an average of 0.99, indicating that weathering-induced dissolution and precipitation were minimal. This probably means an absence of a strong oxidative environment.

The Rb/K ratio exhibits an upward trend in conjunction with rising salinity. The values exceeding 0.006 indicate fully Marine conditions, while those ranging from 0.004 to 0.006 suggest conditions of fresh to brackish water. The values less than 0.004 indicate freshwater conditions [90]. The Rb/K ratio in the Ghahavand sediment ranges from 0.0030 to 0.0049 with an average of 0.0043, indicating that the sediment of the Ghahavand
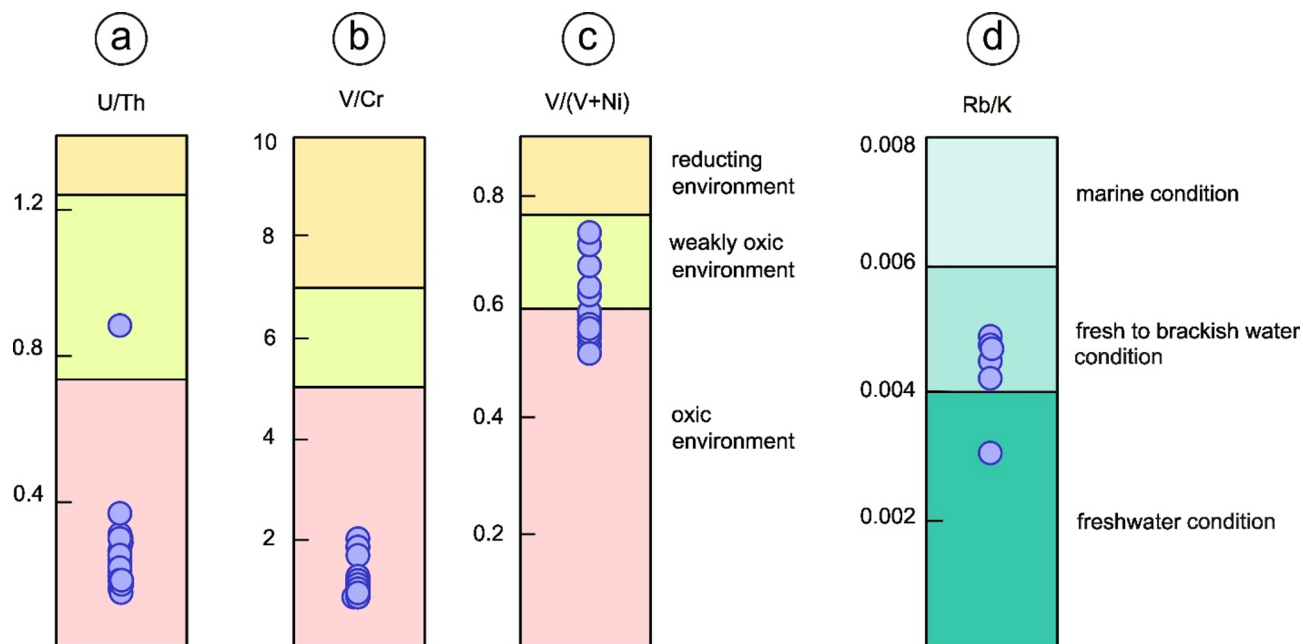
Fig. 12. (**a-b**) Oxidation-reduction condition based on U/Th and V/Cr ratios. Using the discrimination field of Jones and Manning [89], the U/Th and V/Cr ratios indicate that most samples from the Ghahavand area fall within the oxic environment with only one exception. (**c**) Oxidation-reduction state from V/(V+Ni) ratio. The V/(V+Ni) ratio, also interpret using the discrimination field of Hatch and Leventhal [87], support oxic to weakly oxic condition in the Ghahavand Plain sediments. (d) Paleosalinity interference from Rb/K ratio. Based on classification of Ferriday and Montenari [93], the Rb/K ratio in Ghahavand sediments, suggest deposition in fresh to fresh to brackish environment with no evidence of marine influence.

area originates from fresh water and fresh to brackish water and was formed in terrestrial marine-terrestrial sedimentary environments (Fig. 12d).

Conclusions

In this research, we investigate the sediments in the Ghahavand clay flat to assess their potential as a source of lithium (Li). The Ghahavand Plain sediments are notable for containing Lithium-bearing minerals including zebuyelite and psedoeucryptite. The Lithium concentration in this region ranges from 30 to 102 ppm with an average of 55.1 ppm. The third factor in the third step of the factor analysis indicates a strong correlation of Li, Sr, and U. Geochemical characteristics of the Ghahavand Plain sediments such as Ga/Rb and Sr/Cu ratios suggest that the sediments were formed in a cool and arid environment Additionally, the ratios of U/Th, V/Cr, and V/(V + Ni) suggest an oxic environment for the sediment formation. The chemical and Sr isotopic compositions of the sediments reflect a mixture of volcanic and carbonate clay sources, including the Alvand granites, the Eocene-Oligocene volcanic rock, and the Oligomiocene limestone in the surrounding area. Furthermore, the findings underscore the potential for future advancements in technologies aimed at the exploration and exploitation of low-grade lithium deposits. Such progress could make a substantial contribution to the local economy and enhance the scientific understanding of sedimentary processes in arid environments. The geochemical signatures observed in the Ghahavand Plain sediments provide valuable insights into the paleoenvironmental conditions and the geological history of the region. Continued research in this area is likely to reveal additional resources and further elucidate the complex interactions between geological formations and climatic factors.

Data availability

All data associated with this research are available in supplementary file and they can also be requested to the corresponding author.

References

1. Ma, Y., Wang, Y., Yan, G., Yuan, F. & Zhang, W. Synthesis and electrochemical characteristics of flower-like Ca-doped Li4Ti5O12 as anode material for lithium-ion batteries. *Powder Technol.* **407**, 117652 (2022).
2. Shi, C. et al. Enhanced electrochemical performance of the fluidization separation graphite powders from waste power lithium-ion batteries by phenolic resin carbon coated. *Powder Technol.* **411**, 117921 (2022).
3. Talens Peiró, L., Villalba Méndez, G. & Ayres, R. U. Lithium: sources, production, uses, and recovery outlook. *Jom* **65**, 986–996 (2013).

4. Gruber, P. W. et al. Global lithium availability: A constraint for electric vehicles? *J. Ind. Ecol.* **15**, 760–775 (2011).
5. Bradley, D. C., Stillings, L. L., Jaskula, B. W., LeeAnn, M. & McCauley Andrew. D. Critical Mineral Resources of the United States— Economic and Environmental Geology and Prospects for Future Supply, Lithium, Chapter K. in USGS 34 (2017).
6. Wen, H. J. et al. Carbonate-hosted clay-type lithium deposit and its prospecting significance. *Chin. Sci. Bull.* **65**, 53–59 (2020).
7. Benson, T. R., Coble, M. A., Rytuba, J. J. & Mahood, G. A. Lithium enrichment in intracontinental rhyolite magmas leads to Li deposits in caldera basins. *Nat. Commun.* **8**, 270 (2017).
8. Castor, S. B. & Henry, C. D. Lithium-rich claystone in the McDermitt caldera, nevada, USA: geologic, mineralogical, and geochemical characteristics and possible origin. *Minerals* **10**, 1–38 (2020).
9. Foshag, W. F. & Woodford, A. O. Bentonitic Magnesian clay mineral from California. *Am. Mineralogist: J. Earth Planet. Mater.* **21**, 238–244 (1936).
10. Dessemond, C., Lajoie-Leroux, F., Soucy, G., Laroche, N. & Manan, J. F. Spodumene: the lithium market, resources and processes. *Minerals* **334**, 1–17 (2019).
11. Kesler, S. E. et al. Global lithium resources: relative importance of pegmatite, Brine and other deposits. *Ore Geol. Rev.* **48**, 55–69 (2012).
12. Xie, R. et al. Review of the research on the development and utilization of clay-type lithium resources. *Particuology* **87**, 46–53 (2024).
13. Ildoromi, A. Investigation of the role of geomorphology and its application in identification and sustainable development of desert areas (Case study on desert area of hamedan, Iran). *Ann. Biol. Res.* **3**, 1623–1628 (2012).
14. Stöcklin, J. Structural history and tectonics of iran: a review. *Am. Assoc. Pet. Geol. Bull.* **52**, 1229–1258 (1968).
15. Verley, C. G., Videl, M. F. & MaczNeil, E. Report on the Sonora Lithium Project. (2012).
16. Mirzavand, M., Sadeghi, S. H. & Bagheri, R. Groundwater and soil salinization and geochemical evolution of Femenin-Ghahavand plain, Iran. *Environ. Sci. Pollut. Res.* **27**, 43056–43066 (2020).
17. Emami, M. H. Geological map of Qom, 1:25000. N. E6. Preprint at (1978).
18. Bolouchi, M. H. & Hajian, J. The 1:250000 geological map of Kaboudar Ahang. No. D5. Preprint at (1979).
19. Nogol Sadat, A. A. & Hushmanzadeh, A. The 1:250000 geological map of Saveh. No. E5. Preprint at (1984).
20. Amidi, M. & Majidi, B. Geological map of Hamedan, 1:25000. No. D6. Preprint at (1977).
21. Azizi, H. et al. O–Hf isotope ratios of Alvand S-type granite, Western iran, reveal crustal melting in an extensional regime. *Lithos* **464–465**, 107437 (2024).
22. Sheikhi Gheshlaghi, R. et al. The origin of gem spodumene in the Hamadan pegmatite, Alvand plutonic complex, Western Iran. *Can. Mineral.* **60**, 249–266 (2022).
23. Sepahi, A. A., Salami, S., Lentz, D., McFarlane, C. & Maanijou, M. Petrography, geochemistry, and U–Pb geochronology of pegmatites and aplites associated with the Alvand intrusive complex in the Hamedan region, Sanandaj–Sirjan zone, Zagros orogen (Iran). *Int. J. Earth Sci.* **107**, 1059–1096 (2018).
24. Amini, B. & Emami, M. H. Geology map of Iran, scale 1:10000. Preprint at (1996).
25. Morley, C. K. et al. Structural development of a major late cenozoic basin and transpressional belt in central iran: the central basin in the Qom-Saveh area. *Geosphere* **5**, 325–362 (2009).
26. Zheng, M., Liu, W. & Xiang, J. On the discovery of a new mineral—Zabuyelite (Li$_2$CO$_3$). *Acta Mineral. Sinica.* **9**, 155–159 (1989).
27. Taylor, S. R. & McLennan, S. M. *The Continental Crust: its Composition and Evolution* (Blackwell Scientific Pub., 1985).
28. McDonougha, W. F. & Sun, S. The composition of the Earth. *Chem. Geol.* **120**, 223–253 (1995).
29. Yousefi, M., Kamkar-Rouhani, A. & Carranza, E. J. M. Application of staged factor analysis and logistic function to create a fuzzy stream sediment geochemical evidence layer for mineral prospectivity mapping. *Geochem.: Explor. Environ., Anal.* **14**, 45–58 (2014).
30. Yousefi, M. & Carranza, E. J. M. Prediction-area (P-A) plot and C-A fractal analysis to classify and evaluate evidential maps for mineral prospectivity modeling. *Comput. Geosci.* **79**, 69–81 (2015).
31. Reimann, C., Filzmoser, P. & Garrett, R. G. Factor analysis applied to regional geochemical data: problems and possibilities. *Appl. Geochem.* **17**, 185–206 (2002).
32. Steinskog, D. J., Tjøtheim, D. B. & Kvamstø, N. G. A cautionary note on the use of the Kolmogorov-Smirnov test for normality. *Mon Weather Rev.* **135**, 1151–1157 (2007).
33. Kaiser, H. F. The varimax criterion for analytic rotation in factor analysis. *Psychometrika* **23**, 187–200 (1958).
34. Davis, J. C. & Sampson, R. J. & others. Statistics and Data Analysis in Geology. vol. 646Wiley New York, (1986).
35. Qingfei, W. et al. Multifractal analysis of element distribution in skarn-type deposits in the Shizishan orefield, Tongling area, Anhui province, China. *Acta Geologica Sinica-English Ed.* **82**, 896–905 (2008).
36. Sanderson, D. J., Roberts, S. & Gumiel, P. A fractal relationship between vein thickness and gold grade in drill core from La codosera, Spain. *Econ. Geol.* **89**, 168–173 (1994).
37. Mandelbrot, B. B. Self-affine fractals and fractal dimension. *Phys. Scr.* **32**, 257–260 (1985).
38. Deng, J. et al. Delineation and explanation of geochemical anomalies using fractal models in the Heqing area, Yunnan province, China. *J. Geochem. Explor.* **105**, 95–105 (2010).
39. Mandelbrot, B. B. *The Fractal Geometry of Nature* (Time books, 1983).
40. Huh, Y., Chan, L. H. & Edmond, J. M. Lithium isotopes as a probe of weathering processes: orinoco river. *Earth Planet. Sci. Lett.* **194**, 189–199 (2001).
41. Kesler, S. E. et al. Global lithium resources: relative importance of pegmatite, Brine and other deposits. *Ore Geol. Rev.* **48**, 55–69 (2012).
42. Misra, S. & Froelich, P. N. Lithium isotope history of cenozoic seawater: changes in silicate weathering and reverse weathering. *Sci. (1979).* **335**, 818–823 (2012).
43. Teng, F. Z. et al. Lithium isotopic composition and concentration of the upper continental crust. *Geochim. Cosmochim. Acta.* **68**, 4167–4178 (2004).
44. Dellinger, M. et al. Riverine Li isotope fractionation in the Amazon river basin controlled by the weathering regimes. *Geochim. Cosmochim. Acta.* **164**, 71–93 (2015).
45. Li, Q. et al. Hydrochemistry, distribution and formation of lithium-rich Brines in salt lakes on the Qinghai-Tibetan plateau. *Minerals* **9**, 1–15 (2019).
46. Stanley, C. J. et al. LiNaSiB3O7(OH), a new mineral species from the Jadar basin, Serbia. *Eur. J. Mineral.* **19**, 575–580 (2007). Jadarite.
47. Glanzman, R. K., McCarthy, J. H. & Rytuba, J. J. Lithium in the McDermitt Caldera, Nevada and oregon. in Lithium Needs and Resources (ed. Penner, S. S.) 347–353 (Pergamon, 1978). https://doi.org/10.1016/B978-0-08-022733-7.50019-8
48. Zhu, L., Gu, H., Wen, H. & Yang, Y. Lithium extraction from clay-type lithium resource using ferric sulfate solutions via an ion-exchange leaching process. *Hydrometallurgy* **206**, 105759 (2021).
49. Algeo, T. J. & Maynard, J. B. Trace-element behavior and redox facies in core shales of upper Pennsylvanian Kansas-type cyclothems. *Chem. Geol.* **206**, 289–318 (2004).
50. Kesler, S. E. et al. Global lithium resources: relative importance of pegmatite, Brine and other deposits. *Ore Geol. Rev.* **48**, 55–69 (2012).
51. Li, J., Yan, Q., Li, P. & Ivan Jacobson, M. Formation of granitic pegmatites during orogenies: indications from a case study of the pegmatites in China. *Ore Geol. Rev.* **156**, 105391 (2023).

52. Zou, J. et al. Enrichment of critical elements (Li-Ga-Nb-Ta-REE-Y) in the coals and host rocks from the Daping mine, Yudongnan coalfield, SW China. *Ore Geol. Rev.* **152**, 105245 (2023).

53. Dai, S. et al. Chemical and mineralogical compositions of silicic, mafic, and alkali Tonsteins in the late permian coals from the Songzao coalfield, chongqing, Southwest China. *Chem. Geol.* **282**, 29–44 (2011).

54. Calmus, T., Valencia-Moreno, M., Río-Salas, D., Ochoa-Landín, R., Mendivil-Quijada, H. & L. & A multi-elemental study to Establish the natural background and geochemical anomalies in rocks from the Sonora river upper basin, NW Mexico. *Revista Mexicana De Ciencias Geologicas.* **35**, 158–167 (2018).

55. Adepoju, S. A., Ojo, O. J., Akande, S. O. & Sreenivas, B. Petrographic and geochemical constraints on petrofacies, provenance and tectonic setting of the upper cretaceous sandstones, Northern Bida basin, north-central Nigeria. *J. Afr. Earth Sc.* **174**, 104041 (2021).

56. Cullers, R. L. The geochemistry of shales, siltstones and sandstones of Pennsylvanian–Permian age, colorado, USA: implications for provenance and metamorphic studies. *Lithos* **51**, 181–203 (2000).

57. Roser, B. P. & Korsch, R. J. Determination of tectonic setting of sandstone-mudstone suites using SiO2 content and K2O/Na2O ratio. *J. Geol.* **94**, 635–650 (1986).

58. Roser, B. P. & Korsch, R. J. Provenance signatures of sandstone-mudstone suites determined using discriminant function analysis of major-element data. *Chem. Geol.* **67**, 119–139 (1988).

59. Hayashi, K. I., Fujisawa, H., Holland, H. D. & Ohmoto, H. Geochemistry of ~1.9 Ga sedimentary rocks from Northeastern labrador, Canada. *Geochim. Cosmochim. Acta.* **61**, 4115–4137 (1997).

60. McLennan, S. M., Hemming, S., McDaniel, D. K. & Hanson, G. N. Geochemical Approaches to Sedimentation, Provenance, and Tectonics. (1993).

61. Bhatia, M. R. Plate tectonics and geochemical composition of sandstones. *J. Geol.* **91**, 611–627 (1983).

62. Herron, M. M. Geochemical classification of terrigenous sands and shales from core or log data. *J. Sediment. Res.* **58**, 820–829 (1988).

63. Condie, K. C. Chemical composition and evolution of the upper continental crust: Contrasting results from surface samples and shales. *Chem Geol* **104**, 1–37 (1993).

64. Kelts, K. Lacustrine basin analysis and correlation by strontium isotope stratigraphy. Abstract of 13rd International Sedimentary (1987).

65. Shahbazi, H. et al. The Almogholagh pluton, Sanandaj-Sirjan zone, iran: geochemistry, U-(Th)-Pb titanite geochronology and implications for its tectonic evolution. *Neues Jahrbuch Für Mineralogie - Abhandlungen.* **192**, 85–99 (2015).

66. Nouri, F., Azizi, H., Asahara, Y. & Stern, R. J. A new perspective on cenozoic calc-alkaline and shoshonitic volcanic rocks, Eastern Saveh (central Iran). *Int. Geol. Rev.* **63**, 476–503 (2021).

67. McArthur, J. M., Howarth, R. J. & Bailey, T. R. Strontium isotope stratigraphy: LOWESS version 3: best fit to the marine Sr-isotope curve for 0–509 Ma and accompanying look-up table for deriving numerical age. *J. Geol.* **109**, 155–170 (2001).

68. Bradley, D., Munk, L., Jochens, H., Hynek, S. & Labay, K. A. A preliminary deposit model for lithium brines. U.S. Geological Survey Open-File Report 2013–1006 6 (2013).

69. Galarraga, F. et al. V/Ni ratio as a parameter in palaeoenvironmental characterisation of nonmature medium-crude oils from several Latin American basins. *J. Pet. Sci. Eng.* **61**, 9–14 (2008).

70. Yandoka, B. M. S., Abdullah, W. H., Abubakar, M. B., Hakimi, M. H. & Adegoke, A. K. Geochemical characterisation of early cretaceous lacustrine sediments of bima formation, Yola Sub-basin, Northern Benue trough, NE nigeria: organic matter input, preservation, paleoenvironment and palaeoclimatic conditions. *Mar. Pet. Geol.* **61**, 82–94 (2015).

71. Roy, D. K. & Roser, B. P. Climatic control on the composition of Carboniferous-Permian Gondwana sediments, Khalaspir basin, Bangladesh. *Gondwana Res.* **23**, 1163–1171 (2013).

72. Beckmann, B., Flögel, S., Hofmann, P., Schulz, M. & Wagner, T. Orbital forcing of cretaceous river discharge in tropical Africa and ocean response. *Nature* **437**, 241–244 (2005).

73. Xu, Q. et al. Geological and geochemical characterization of lacustrine shale: A case study of the jurassic da'anzhai member shale in the central Sichuan basin, Southwest China. *J. Nat. Gas Sci. Eng.* **47**, 124–139 (2017).

74. Lerman, A. & Lakes *Chemistry, Geology, Physics* (Springer, 1989).

75. Balaram, V. et al. A review of applications, occurrence, exploration, extraction, recycling, analysis, and environmental impact. *Geosci. Front.* **15**, 101868 (2024).

76. Ann Munk, L. et al. Lithium brines: origin, characteristics, and global distribution. *Econ. Geol.* https://doi.org/10.5382/econgeo.5134 (2025).

77. Meixner, A., Alonso, R. N., Lucassen, F., Korte, L. & Kasemann, S. A. Lithium and Sr isotopic composition of Salar deposits in the central Andes across space and time: the Salar de pozuelos, Argentina. *Min. Depos.* **57**, 255–278 (2022).

78. Szlugaj, J. & Radwanek-Bąk, B. Lithium sources and their current use. *Gospodarka Surowcami Mineralnymi / Mineral. Resour. Manage.* **38**, 61–88 (2022).

79. Nesbitt, H. W. & Young, G. M. Prediction of some weathering trends of plutonic and volcanic rocks based on thermodynamic and kinetic considerations. *Geochim Cosmochim Acta* **48**, 1523–1534 (1984).

80. Nesbitt, H. W. & Young, G. M. Formation and diagenesis of weathering profiles. *J. Geol.* **97**, 129–147 (1989).

81. Jaiswal, M. K., Srivastava, P., Tripathi, J. K. & Islam, R. Feasibility of the Sar technique on quartz sand of terraces of NW himalaya: A case study from Devprayag. *Geochronometria* **31**, 45–52 (2008).

82. Fang, Z. et al. Geochemical Insights into the Cambrian Wulongqing Formation, Yangtze Plate: Tracing Provenance and Paleoweathering. *Minerals* 15, (2025).

83. Nesbitt, H. W. & Young, G. M. Early proterozoic climates and plate motions inferred from major element chemistry of lutites. *Nature* **299**, 715–717 (1982).

84. Bai, Y. et al. Rare Earth and major element geochemistry of eocene fine-grained sediments in oil shale-and coal-bearing layers of the Meihe basin, Northeast China. *J. Asian Earth Sci.* **97**, 89–101 (2015).

85. Fedo, C. M., Nesbitt, W., Young, G. M. & H. & Unraveling the effects of potassium metasomatism in sedimentary rocks and paleosols, with implications for paleoweathering conditions and provenance. *Geology* **23**, 921–924 (1995).

86. Kesler, S. E., Simon, A. C. & Simon, A. F. *Mineral Resources, Economics and the Environment* (Cambridge University Press, 2015).

87. Hatch, J. R. & Leventhal, J. S. Relationship between inferred redox potential of the depositional environment and geochemistry of the upper Pennsylvanian (Missourian) Stark shale member of the Dennis limestone, Wabaunsee county, kansas, U.S.A. *Chem. Geol.* **99**, 65–82 (1992).

88. Rimmer, S. M., Thompson, J. A., Goodnight, S. A. & Robl, T. L. Multiple controls on the preservation of organic matter in Devonian–Mississippian marine black shales: geochemical and petrographic evidence. *Palaeogeogr Palaeoclimatol Palaeoecol.* **215**, 125–154 (2004).

89. Jones, B. & Manning, D. A. C. Comparison of geochemical indices used for the interpretation of Palaeoredox conditions in ancient mudstones. *Chem. Geol.* **111**, 111–129 (1994).

90. Mongenot, T., Tribovillard, N. P., Desprairies, A., Lallier-Vergès, E. & Laggoun-Defarge, F. Trace elements as palaeoenvironmental markers in strongly mature hydrocarbon source rocks: the cretaceous La Luna formation of Venezuela. *Sediment. Geol.* **103**, 23–37 (1996).

91. Akinlua, A., Adekola, S. A., Swakamisa, O., Fadipe, O. A. & Akinyemi, S. A. Trace element characterisation of cretaceous orange basin hydrocarbon source rocks. *Appl. Geochem.* **25**, 1587–1595 (2010).

92. van der Weijden, C. H. & van der Weijden, R. D. Mobility of major, minor and some redox-sensitive trace elements and rare-earth elements during weathering of four granitoids in central Portugal. *Chem Geol* **125**, 149–167 (1995).
93. Ferriday, T. & Montenari, M. Chemostratigraphy and chemofacies of source rock analogues: A high-resolution analysis of black shale successions from the Lower Silurian Formigoso Formation (Cantabrian Mountains, NW Spain). In *Stratigraphy & Timescales* **1** 123–255 (2016).

Acknowledgements

Author contributions

ND and HA. Made fieldwork, sampling, wrote the main manuscript text, and prepared the figures. ND, HA, MM, YA, and MT conducted whole rocks chemistry and isotope analyses. ND and MM made XRD analysis. All authors reviewed, revised, and edited the text and table at each stage.

Declarations

Competing interests

The authors declare no competing interests.

Additional information

Supplementary Information The online version contains supplementary material available at https://doi.org/10.1038/s41598-025-18536-3.

Correspondence and requests for materials should be addressed to H.A.

Reprints and permissions information is available at www.nature.com/reprints.

Publisher's note Springer Nature remains neutral with regard to jurisdictional claims in published maps and institutional affiliations.